Nanoscale membrane curvature sorts lipid phases and alters lipid diffusion

Woodward, Xinxin; Javanainen, Matti; Fabian, Balazs; Kelly, Christopher

2023-06-06
Elsevier B.V.
http://hdl.handle.net/10138/576605
Woodward, X, Javanainen, M, Fabian, B & Kelly, C 2023, 'Nanoscale membrane curvature sorts lipid phases and alters lipid diffusion', Biophysical Journal, vol. 122, no. 11, pp. 2203-2215. https://doi.org/10.1016/j.bpj.2023.01.001

Nanoscale membrane curvature sorts lipid phases and alters lipid diffusion

Xinxin Woodward[1], Matti Javanainen[2,3], Balázs Fábián[2], Christopher V. Kelly[1,*]

[1]Department of Physics and Astronomy, Wayne State University, Detroit, MI, U.S.A. 48201
[2]Institute of Organic Chemistry and Biochemistry, Czech Academy of Sciences, Prague, Czech Republic, 16000
[3]Institute of Biotechnology, University of Helsinki, Helsinki, Finland, 00014
* To whom correspondence should be addressed. E-mail: cvkelly@wayne.edu

Significance Statement

Nanoscopic membrane organization and dynamics are critical for cellular function but challenging to experimentally measure. This work brings together super-resolution optical methods with multiscale computational approaches to reveal the interplay between curvature, composition, phase, and diffusion in model membranes. Nanoscale membrane curvature induced phase separation in otherwise homogeneous membranes, and the phase-curvature coupling had a direct implication on lipid mobility. This discovery advances understanding of the fundamental membrane biophysics that regulate membrane activities such as endocytosis and viral budding.

Keywords

Membrane curvature; single-particle tracking; lipid phase separation; molecular sorting; diffusion

Abstract

The precise spatiotemporal control of nanoscale membrane shape and composition is the result of complex interplay of individual and collective molecular behaviors. Here, we employed single-molecule localization microscopy and computational simulations to observe single-lipid diffusion and sorting in model membranes with varying compositions, phase, temperature, and curvature. Supported lipid bilayers were created over 50-nm radius nanoparticles to mimic the size of naturally occurring membrane buds, such as endocytic pits and the formation of viral envelopes. The curved membranes recruited liquid-disordered lipid phases while altering the diffusion and sorting of tracer lipids. Disorder-preferring fluorescent lipids sorted to and experienced faster diffusion on the nanoscale curvature only when embedded in a membrane capable of sustaining lipid phase separation at low temperatures. The curvature-induced sorting and faster diffusion even occurred when the sample temperature was above the miscibility temperature of the planar membrane, implying that the nanoscale curvature could induce phase separation in otherwise homogeneous membranes. Further confirmation and understanding of these results are provided by continuum and coarse-grained molecular dynamics simulations with explicit and spontaneous curvature-phase coupling, respectively. The curvature-induced membrane compositional heterogeneity and altered dynamics were achieved only with a coupling of the curvature with a lipid phase separation. These cross-validating results demonstrate the complex interplay of lipid phases, molecular diffusion, and nanoscale membrane curvature that are critical for membrane functionality.

Introduction

Cell plasma membranes contain thousands of distinct lipid species with spatial heterogeneity in composition and shape. Natural membrane compositions near a phase coexistence manifest functional membrane domains that are more and less structured and resemble liquid ordered (L_o) and liquid disordered (L_d) phases (1–4). Membrane domains are critical for cell functions such as protein sorting, cell signaling, membrane budding, and retrovirus replication through the regulation of local variations in the membrane composition (4–8). Caveolae, for example, are cholesterol and sphingolipid-rich endocytic buds that have diverse roles in membrane compositional regulation, trafficking, force sensing, and endocytosis on the sub-100-nm length scale (9–11). The coupling of membrane phases and curvature on live cells remains unconfirmed yet likely crucial for diverse cellular functions.

Model membranes of known lipid mixtures provide a means to reveal how the membrane composition affects function. Coexisting L_o and L_d phases can be created by combining a sterol, a phospholipid with a high chain-melting temperature, and a phospholipid with a low chain-melting temperature below the mixture's miscibility transition temperature (T_{mix}) (12, 13). Phase-separated model membranes have shown curvature-dependent phase separations in tubules (14–17), small vesicles (18), and supported lipid bilayers (SLBs) (19–21). In select cases, the membrane shape has been shown to induce a phase separation that was not observed on planar membranes (14, 15). In model membranes, the region of greater curvature (*i.e.,* smaller radius) concentrates disordered lipids as the L_d phase has a lower bending rigidity than the L_o phase (22). Interestingly, however, endocytic processes and viral budding in live cells are typically correlated with L_o-preferring lipids, such as cholesterol and sphingomyelin (23), which may occur if the area of the ordered phase is significantly smaller than the disordered phase or if the order-preferring lipids and proteins have a greater spontaneous curvature (24). Typically, single lipids are too small relative to the membrane curvature for the curvature to significantly alter their distribution in the membrane without the collective action of lipid phases (18, 25–27). The physical principles that govern the sorting of lipids to <100-nm membrane buds remain a mystery fundamental to both cellular homeostasis and pathophysiology. This manuscript reports the temperature-dependent diffusion and sorting on membranes to better understand the interplay of lipid mobility, phase separation, and curvature.

Lipid diffusion in the L_d phase is up to 10x faster than lipids in the L_o phase, depending on the membrane composition, the fluorescent lipids tracked, and the substrate topography (28–33). For example, DPPE-Texas Red in SLBs composed of DiPhyPC, DPPC, and cholesterol at molar ratios of 2:2:1 had a diffusion coefficient (1.8 ± 0.5)x greater in the L_d phase than the L_o phase (34). The diffusion in the two phases became indistinguishable when the sample is near or above T_{mix}, which can occur with increasing the temperature or cholesterol content, as is associated with shorter tie-lines separating the phases. For example, SLBs composed of DiPhyPC, DPPC, and cholesterol at molar ratios of 1:1:2 demonstrated lipid phase separation, as evident by the partitioning of DPPE-Texas Red, but no difference in the DPPE-Texas Red diffusion was observed between the two phases (34).

Experimental limitations and the underlying topological manifold result in the motion of particles on curved membranes appearing non-Brownian (35). Restrictions on the observable lag times and localizations precision result in the measured diffusion becoming increasingly non-local, in the sense that observed particle motion averages patches of the membrane. Consequently, the lipid mobility

becomes reflective of the average membrane environment with a loss of nanoscale information. Nonetheless, modern single-particle localization and computational methods are converging to reveal spatially varying membrane behaviors at physiological length scales.

The influence of membrane curvature on single-lipid diffusion has been studied in well-defined geometries. Diffusion typically slows on cylindrical membranes when the radii are smaller than 50 nm (36). But the effects of curvature on lipid diffusion are correlated to the fluorophore location on the labeled lipid; head-group-labeled lipids diffuse 3x faster on flat versus curved membranes, whereas tail-labeled lipids diffuse at the same rate on flat and curved membranes (37). Recent experimental and computational capabilities to measure diffusion and sorting at the nanoscale are beginning to reveal an intertwined network of contributing factors affecting membrane phenomena, including the effects of hydrodynamics, geometry, projection, lipid packing, and measurement time. For example, membrane curvature affects the thickness, area-per-lipid, and the order parameter of the lipid hydrocarbon chains (38).

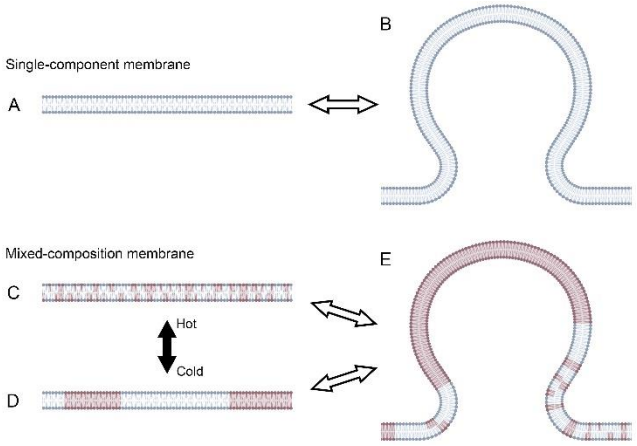

Figure 1:
(A, B) Single-component membranes have no apparent redistribution of fluorescent lipids and minimal or fluorophore-dependent curvature dependence on the single-lipid diffusion. (C-E) Membranes of mixed composition, however, may have temperature-dependent phase separation that couples to the membrane shape. At temperatures both (C) above and (D) below T_{mix}, a L_d phase may sort to (E) the more curved regions in model membranes. This manifests as faster single-lipid diffusion correlated with the curved membrane with lipids diffusing faster in L_d than L_o phases.

In this manuscript, the diffusion and sorting of lipids relative to nanoscale membrane curvature and phase separation are quantified with experimental and computational methods. Single-component membranes displayed negligible changes to the local membrane composition or dynamics relative to membrane curvature (Fig. 1A, B). Membranes of mixed composition demonstrated sorting of a L_d phase to the nanoscale curvature regardless of if the planar membrane was above or below T_{mix} (Fig. 1C-E). These results were observed experimentally and computationally by fluorophore sorting, single-lipid diffusion, coarse-grained molecular dynamics, and continuum simulations. Membrane curvature was experimentally generated by creating phase-separated SLBs over 50-nm radius nanoparticles on planar microscopy coverslips (Fig. 2). The concentration of DPPE-Texas Red on the curved membrane was measured *via* diffraction-limited images and analyzed for lipid sorting. Single-molecule localization microscopy and single-particle tracking (SPT) were performed to track individual DPPE-Texas Red

molecules and to measure their curvature- and phase-dependent mobility. The disorder-preferring fluorescent lipids were more concentrated on the curved membrane than the surrounding planar bilayer when embedded in a membrane capable of sustaining lipid phase separation. This sorting occurred regardless of the phase of the immediately surrounding bilayer, but sorting was more pronounced if the membrane bud was immediately surrounded by a L_o phase. The single-lipid diffusion was up to 2.2x faster on curved versus planar membranes, with a dependence on the length of the phase-separating tie-lines. These experimental results were verified in computational simulations of phase separation, including continuum and molecular dynamics simulations with explicit or spontaneous phase-curvature coupling, respectively. The sorting of disorder-preferring lipids to the curvature and the effects of the curvature propagating onto the surrounding planar membrane were consistently observed with the curvature site acting to seed lipid phase separation for larger-scale influence over the surrounding membrane's average phase. Further, the sorting of the lipid phases to curvature sites occurred even when the sample conditions (i.e., composition and temperature) were such as to not induce large-scale phase separation on the planar membrane. This demonstrates how the plasma membrane may appear uniform in composition without large-scale phase separation yet utilize phase separation in the recruitment of membrane-bound molecules to or from endocytic pits.

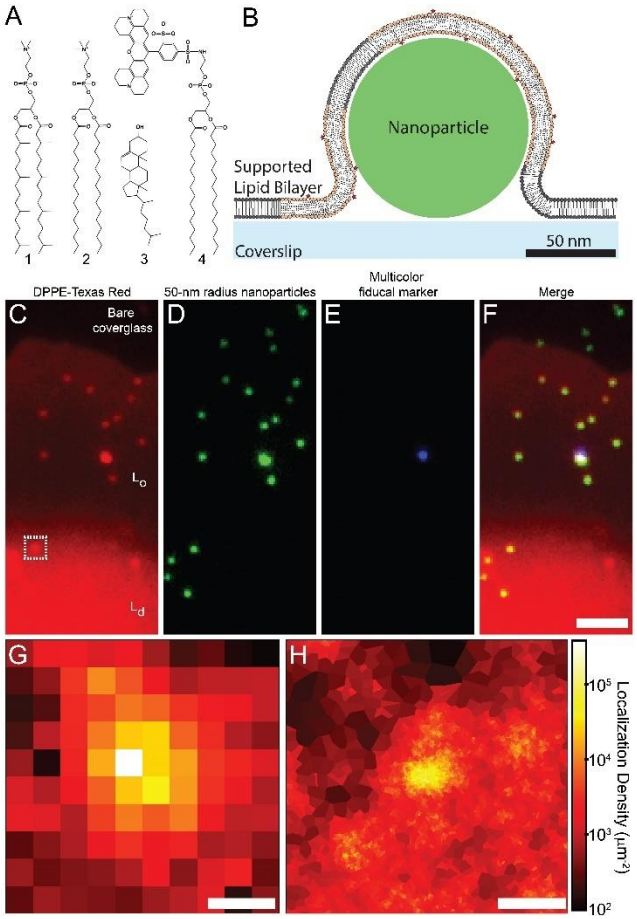

Figure 2:

Phase-separated SLBs were created with nanoscale membrane curvature. (A) The lipids used include (1) DiPhyPC, (2) DPPC, (3) cholesterol, and (4) DPPE-Texas Red. (B) The lipid phases and single-lipid diffusion were experimentally measured relative to the engineered, nanoparticle-induced membrane curvature. (C-H) 1:1:2 molar ratio of DiPhyPC:DPPC:cholesterol and 0.1 mol% DPPE-Texas Red is shown over 50-nm radius nanoparticles. Multi-colored, diffraction-limited fluorescence images include those of (C) DPPE-Texas Red, (D) the 100 nm diameter fluorescent nanoparticles, (E) the multicolored nanoparticle fiducial markers, and (F) their merged image. (C) The phase-separated membrane contained a micron-scale L_d domain (*bright, bottom*) and L_o domain (*dim, middle*) while surrounded by bare coverslip (*black, top*). (G) Diffraction-limited and (H) super-resolution images of the membrane with engineered curvature revealed the sorting and diffusion of lipids from outlined region of (C). Scale bars represent (C-F) 2 µm or (G-H) 200 nm.

Results

Phase separation in planar SLBs

To assess the lipid phases within the membranes, we added fluorescence tracer lipids to ternary mixtures of DiPhyPC, DPPC, and cholesterol. Phase-separated GUVs were burst upon microscopy coverslips to create SLBs patches with distinct lipid phase of similar size as present on the GUVs, *i.e.*, >5 µm wide domains. Bright domains on the membranes indicated the L_d phase, dim domains indicated the L_o phase, and black regions indicated the lack of an SLB over the coverslip (Fig. 2). Substrate-membrane interactions prevented the diffusion of domains in the SLB and the coalescence of optically resolvable lipid phases in SLBs that were created by small vesicle fusion. The fluorescence contrast between the L_o and L_d phases reflects the partition coefficient of the fluorescent lipid and the length of the tie-line that separated the two phases. The L_o and L_d phases were more similar in brightness at higher cholesterol concentrations and at higher temperatures.

The observed T_{mix} varies between SLB patches similar to the variation between GUVs in a sample (39). The T_{mix} for planar SLBs with a molar ratio of 1:1:2 DiPhyPC:DPPC:cholesterol was between 28 °C and 37 °C, as evident by the stable phase separation at 28 °C and the phase mixing at 37 °C (Fig. S1). The T_{mix} for planar 2:2:1 SLBs was greater than 37 °C, as evident by the consistently sharp phase boundaries. All samples were equilibrated for >30 min prior measuring the phase separation or lipid diffusion. The slow large-scale mixing of SLBs resulted in some of the largest domains (>10µm diameter) remaining evident with blurred phase boundaries after equilibration at a temperature greater than T_{mix}, as described previously (34, 40).

Ld-preferring lipids sort to curvature

To measure if nanoscale membrane curvature preferentially recruited lipid phases, we engineered curvature in SLBs by bursting phase-separated GUVs over 50-nm radius nanoparticles and glass coverslips (Fig. 2B). Multicolor imaging provided tracking of the L_d-preferring tracer lipid density (Fig. 2C), the fluorescent, 50-nm radius, membrane-curvature-generating nanoparticles (Fig. 2D), and multi-color fiducial mark (Fig. 2E) to ensure chromatic alignment and confirmation membrane bud locations. This setup provided a nanoengineered membrane shape while allowing individual lipids to diffuse freely within the SLB. The connectivity of the membrane between the planar SLB and the membrane bud over the nanoparticle was demonstrated both with fluorescence recovery after photobleaching and the presence of uninterrupted of single-lipid trajectories (Fig. S2) (26, 41).

Lipid sorting was induced by membrane curvature with disorder-preferring fluorescent lipids concentrating on the curvature (Fig. 3). Quasi-single component POPC and DiPhyPC membranes served as a control and normalization for the phase-independent increase in membrane area per pixel, brightness, and single-molecule sorting to curvature (Eq. S4). In all quasi-single component membranes, no apparent sorting of the fluorescent lipids to the curvature was observed; the local increase in membrane brightness at the bud was consistent with an increase in membrane area projected onto the XY-imaging plane (37).

In mixed-composition membranes, the lipid phase on the curved membrane (P_C) was compared to the phase of the flat membrane (P_F) immediately surrounding each nanoparticle-supported membrane bud (Eqs. S3 and S4). P_C and P_F were measured for varying membrane compositions and temperatures. In SLBs with phase separation, lower temperatures provide a greater range in P_F values, which is consistent with lower temperatures yielding longer tie-lines and a wider variety in the fluorescent lipid density across the membrane (Fig. 3A). The phase on membrane buds was highly correlated with the phase surrounding the bud (Fig. 3B). But the phase on the bud was consistently more disordered than the surrounding phase (Fig. 3C). The sorting of the L_d phase to the curved membrane is evident by P_C being greater than P_F, *i.e.,* with the disorder-preferring probe localizing at curved regions. The ratio of P_C/P_F is analogous to a curvature-dependent partition coefficient and a previously used quantification of phase sorting (15).

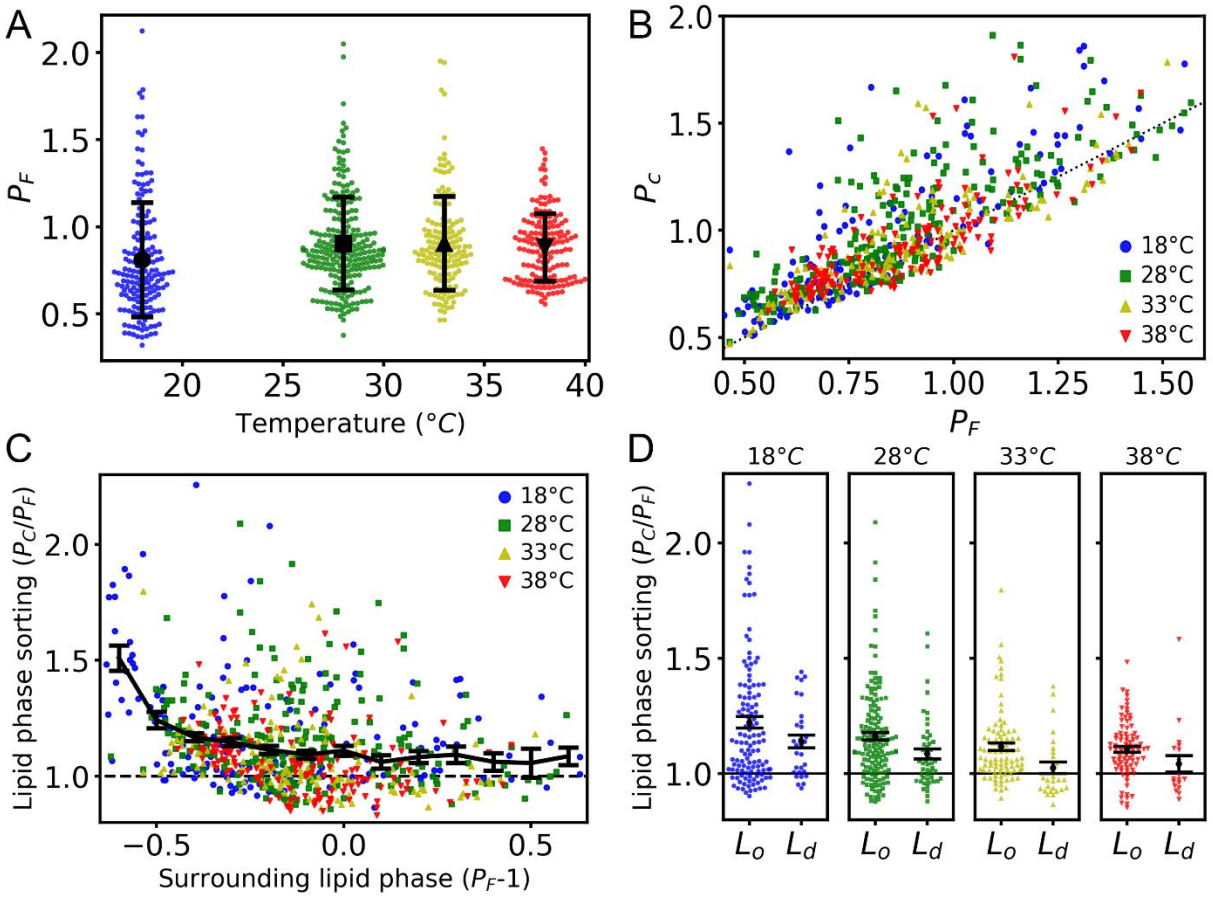

Figure 3:
Curvature-induced phase sorting was observed in SLBs by assessing the phase on the curved and the surrounding flat membrane. Each data point here represents a single membrane bud in a membrane with an average 1:1:2 molar ratio of DiPhyPC:DPPC:cholesterol. (A) A greater range of phase on the flat membrane (P_F) were observed at colder temperatures, consistent with colder temperatures providing longer tie lines; the black data represents the mean and the standard deviation of observations at each temperature. (B) The phase of the curved membrane (P_C) was more likely to be disordered if the surrounding flat area was more disordered; the dotted line represents $P_C = P_F$ to guide the eye. (C) The normalized ratio of curved to flat phases reveals that greater phase sorting is observed when the surrounding membrane was more ordered, show as larger P_C/P_F ratios values when P_F is smaller. Here the black data represents the mean and standard error of P_C/P_F for all temperatures as binned by P_F. (D) Grouping the data based on the $P_F < 0.9$ for L_o and $P_F > 1.1$ for L_d reveals that the L_d phase sorted to the curvature at all temperatures; the black data represents the mean and standard error for each condition.

The P_C/P_F ratio versus P_F for different phase-separating lipid mixtures and temperatures show no clear change in P_C/P_F ratio versus temperature. The P_C/P_F ratio was greater than 1 for all temperatures and all values of P_F, which indicates that the curved membrane was consistently more concentrated in the disorder-preferring fluorescent lipid than the surrounding flat membrane (Fig. 3C). Interestingly, the P_C/P_F ratio was larger when P_F was lower, which reveals that the curvature-induced sorting of lipid phases was strongest when the surrounding phase was more ordered. This is further shown by characterizing the lipid phase sorting for varying temperatures (Fig. 3D). At all temperatures, the buds surrounded by L_o phase showed more curvature-induced sorting than the buds surrounded by the L_d phase, and this is most clear at lower temperatures.

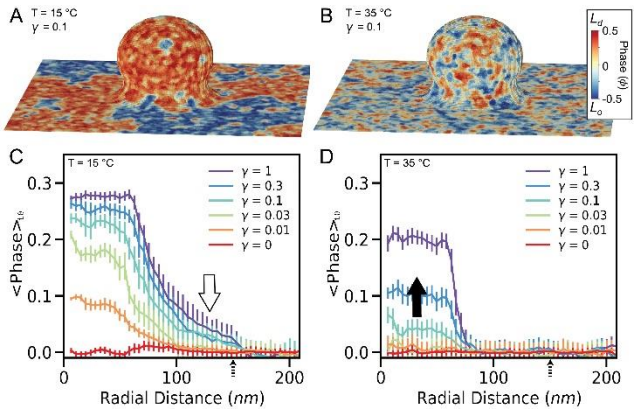

Figure 4:
Continuum simulations that couple lipid phases to curvature were performed incorporating an explicit phase-curvature coupling (γ). (A, B) Representative snapshots and (C,D) the time- (t) and azimuthally (θ) averaged phase reveal the coupling between the temperature (T) and γ. A Landau second-order phase transition was coupled with an effective temperature of (A, C) 15 °C or (B, D) 35 °C. (C) When bulk phase separation is stable, the curvature acts as a nucleation site with the L_d phase concentrating at the curvature and propagating on to the surrounding planar membrane (*white arrow*). (D) When a higher temperature prevents bulk phase separation, a phase-curvature coupling may still induce the sorting of a disordered phase to the membrane bud (*black arrow*). The boundary of $r \geq 150$ nm (*dashed arrow*) was renormalized every frame to have equal L_d and L_o representation (i.e., $\langle phase \rangle_{r>150} = 0$) to avoid the entire simulation from converging to a single phase.

Continuum simulation demonstrate curvature-induced lipid domains

To validate the experimental sorting results, we performed computational simulations of a curved membrane with a local phase governed by the continuum Landau theory and an explicit phase-curvature coupling constant (γ) (Eq. S9). The membrane was modeled to have a topography consistent with the experimental, 50-nm radius, nanoparticle-supported SLBs and divided into 3861 distinct cells each with an area of 9 nm^2 (Fig. S5). Landau phase constants and effective temperatures were chosen to provide two phases with realistic fluctuations in the local composition and phase boundaries, as described in the Supporting Information. Gaussian noise in the phase was added to each cell with each time step to model thermal fluctuations; a larger standard deviation (σ) in this noise represented higher temperature simulations.

At low temperature (σ = 0.07, T = 15 °C), stable domains formed with fluctuations at the phase boundaries (Fig. 4A). At high temperature (σ = 0.08, T = 35 °C), rapid fluctuations resulted in no large or stable phases present on the planar membrane (Fig. 4B). The supplemental material includes movies of these simulations and images of the average phase across the membrane during the simulation with varying temperature and phase–curvature coupling (Movie S1 and Fig. S6). The L_d phase was sorted to the curvature in a σ- and γ-dependent manner. At low temperatures, even weak phase–curvature coupling resulted in significant sorting of the L_d phase to the membrane bud (Fig. 4C). The phase sorting propagated onto the flat membrane surrounding the bud, which resulted in the planar membrane close to the curvature being more likely to be disordered than the planar membrane far from the curvature. The L_d phase was also sorted to the curved membrane even at high temperatures when no large phases were observed on the planar membrane if γ ≥ 0.1 (*black arrow*, Fig. 4D).

This approach does not ensure consistent composition of the membrane during the simulation, *i.e.*, the fraction of the membrane that is L_d may change versus time. Further, this method does not reproduce phase fluctuation dynamics. This approach does allow for convergence of system to equilibrated membrane phase distribution. Accordingly, these simulations are used for revealing phase sorting relative to the curvature and not for diffusion of the lipids. Because the phase–curvature coupling is explicitly included within Eq. S9, the sorting of the L_d is expected. However, consequences of varying temperature and the propagation of the phase sorting to the surrounding planar membrane provided valuable cross-validation of the experimental and MD results that were well represented by the applied Hamiltonian with only a first-order, linear phase–curvature coupling.

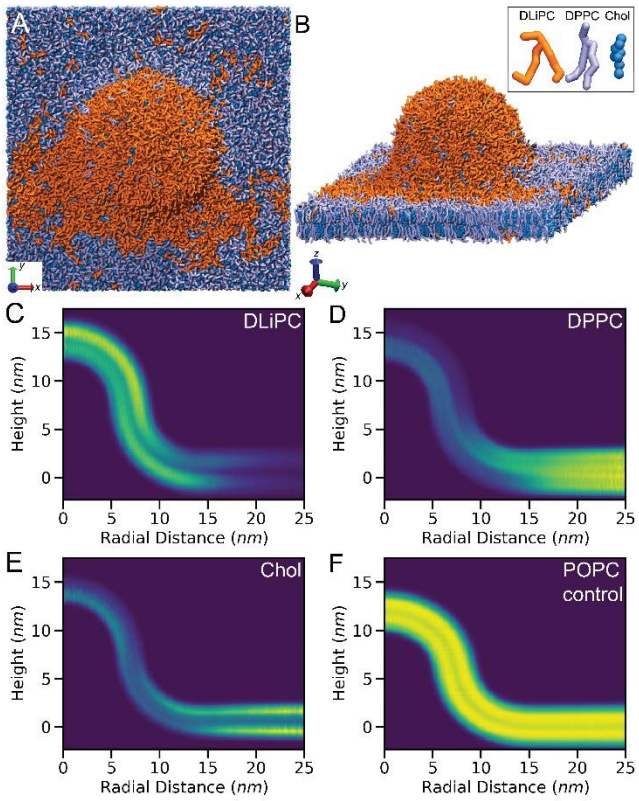

Figure 5:
Coarse-grained molecular dynamics simulations spontaneously demonstrated phase–curvature coupling through lipid sorting and diffusion. (A, B) Coarse-grained simulations of a mixture of DLiPC, DPPC, and cholesterol revealed the coupling of phase separation to membrane curvature. Normalized 2D histograms show the azimuthally averaged density of lipid beads for each lipid type with (C) the L_d-preferring DLiPC concentrating on the bud with the L_o-preferring (D) DPPC and (E) cholesterol relatively concentrating on the flat membrane. (F) POPC-only simulations reveal near uniform lipid densities throughout the simulation.

Molecular dynamics simulations demonstrate spontaneous phase–curvature coupling

To further validate these results, coarse-grained (CG) molecular dynamics simulations were performed with nanoscale membrane curvature maintained by dummy particles (42). CG simulations provide single-molecule dynamics from a particular leaflet of the membrane of known shape without perturbations from fluorescent labels. CG simulations included a 5-nm radius hemispherical bud connected to a planar bilayer with a membrane neck of 5-nm minimum radius of curvature (Fig. 5, Movie S2). The membranes had positive Gaussian curvature on the hemispherical bud top, and negative curvature on the neck (Fig. S8A). The simulated lipids diffused and sorted spontaneously relative with to the constant membrane shape according to the Martini force field (43).

The local concentrations of the individual lipid types were azimuthally averaged and displayed as 2D histograms (Fig. 5C-F), or computed as the real on-surface densities to show the relationship between membrane curvature and leaflet compositions (Fig. S8B). Pure POPC bilayers, which are not capable of inducing a lipid phase separation, demonstrated no significant molecular-scale changes in lipid density with curvature (Fig. 5F). However, for the commonly used phase-separating mixture of DPPC, DLiPC, and cholesterol, the membrane curvature recruited and concentrated the disorder-preferring DLiPC lipids while repelling the order-preferring DPPC and cholesterol. In both leaflets, DLiPC

was concentrated on the hemispherical bud and the neck, consistent with experimental and continuum simulation results. The degree of phase separation of the individual leaflets was distinct, with the upper leaflet inducing a more pronounced sorting (Figs. 5 and S8), with a greater discussion of leaflet asymmetry being the focus of a future study.

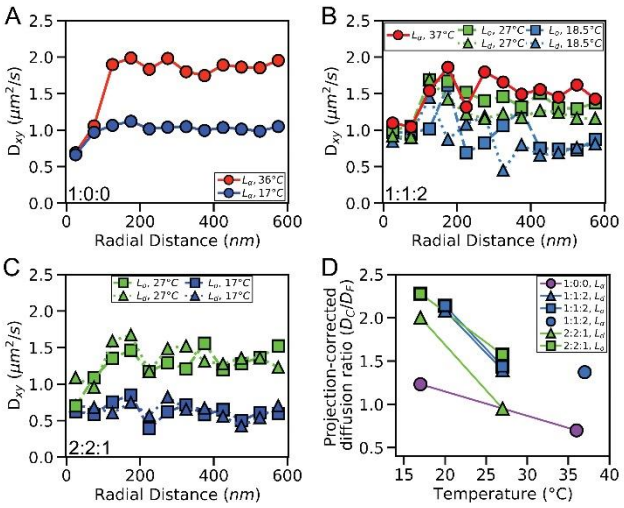

Figure 6:
Curvature and phase separation influence lipid mobility. The lipid diffusion rate as projected into the XY-plane (D_{xy}) was measured versus the radial distance away from the center of the membrane buds for (A) DiPhyPC membrane and phase-separated membranes composed of (B) 1:1:2 or (C) 2:2:1 molar ratio of DiPhyPC:DPPC:cholesterol. Monte Carlo fitting to the diffusion through the XY-plane yielded the in-membrane diffusion rate to extract the local in-membrane diffusion rates by correcting for the effects of projecting the 3D membrane shape into the XY-imaging plane. (D) The ratio of the in-membrane diffusion rates on the curved versus flat membranes (D_C/D_F) are shown for varying membrane composition, phase, and temperature. Uncertainty levels for each data point are given in Table S1.

Single-lipid diffusion demonstrates the phase–curvature coupling

To test the effects of the phase–curvature coupling on lipid diffusion, experimental and computational SPT was performed to correlate the single-lipid dynamics with the membrane topography. The single-lipid trajectories were experimentally observed in SLBs with engineered membrane buds of 50-nm radius. The lipid phase, curvature, and temperature-dependent diffusion of DPPE-Texas Red was measured (Fig. 6). Diffusion was studied for SLBs of 1:0:0, 1:1:2, and 2:2:1 molar ratios of DiPhyPC:DPPC:cholesterol. Each single-lipid step length through the XY-plane was binned based on the radial lateral distance from the center of the membrane bud (r). Rayleigh distribution fitting of the single-step lengths in each bin provided a spatially mapped diffusion coefficient across the topographically varying SLB (37, 41, 44) (Eq. S5). This SPT analysis method provides greater spatial resolution of lipid diffusion than the conventional fluorescence recovery after photobleaching (FRAP) or mean squared displacement (MSD) versus lag time (Δt) analysis (45). FRAP typically reports the mean diffusion over a diffraction-limited region of interest, and MSD vs. Δt typically averages together the diffusers' entire >1 μm trajectories (Fig. S7) (45).

The radially dependent diffusion through the XY-plane (D_{xy}) varied with membrane topography due to both the curvature-dependent lipid mobility and the geometrical effects of projecting the 3D lipid

trajectories into the imaging plane. Without correction, the D_{xy} is smaller on the membrane bud because the lipid diffuses significantly in the Z-direction, which is not detected. It is critical to remove this geometrical consideration from the observed D_{xy} prior to analyzing the diffusion on the curved versus flat membrane. The contribution due projecting the curved membrane on to the XY-imaging plane was estimated from Monte Carlo simulations and subtracted to reveal an effective diffusion rate of the lipids on the curved (D_C) and flat membrane (D_F), as described in the Supporting Information (Eqs. S7 and S8). As the temperature increased, D_F increased, as expected (37, 46–48), showing that hotter membranes display faster diffusion.

To measure the phase- and curvature-dependent lipid diffusion, membrane buds were grouped based on the membrane composition, temperature, and surrounding phase. The individual curvature events were deemed L_d or L_o phase if P_F was greater than 1.1 or less than 0.9, respectively. The curvature-dependent effects on diffusion were calculated through the projection-corrected ratios of D_C/D_F. All values of the D_C/D_F ratios for ternary mixtures were greater than or equal to one; the lipids in phase-separated membranes diffuse faster if the membrane is curved (Fig. 6D). The greatest D_C/D_F ratio was observed in 20 °C SLBs with a 2:2:1 molar ratio of DiPhyPC:DPPC:cholesterol when the buds were surrounded by L_o phase when D_C/D_F = 2.3 ± 1.0. The D_C/D_F ratios were larger at the colder temperatures, consistent with the L_d-preferring lipids sorting to the curvature more when the tie-line separating the phases was longer, as also seen in the continuum models (Fig. 4).

Interestingly, D_{xy} decreased as r increased from 125 nm to 400 nm in ternary mixtures with clear phase separation (*i.e.*, at lower temperatures and higher cholesterol content) (Fig. 6B). The noise in the data makes this trend subtle, but the D_{xy} values for r = 150–200 nm are consistently higher than the data points for r = 350–400 nm. This trend is most obvious for the 1:1:2 composition at 18.5 °C data.

This decreasing D_{xy} on the flat membrane near the curvature may be due to curvature-seeded L_d phase propagation onto the planar SLB surrounding the nanoparticle, as was also seen in both the continuum and CG computational simulations (Figs. 4B, 5C, and 7B).

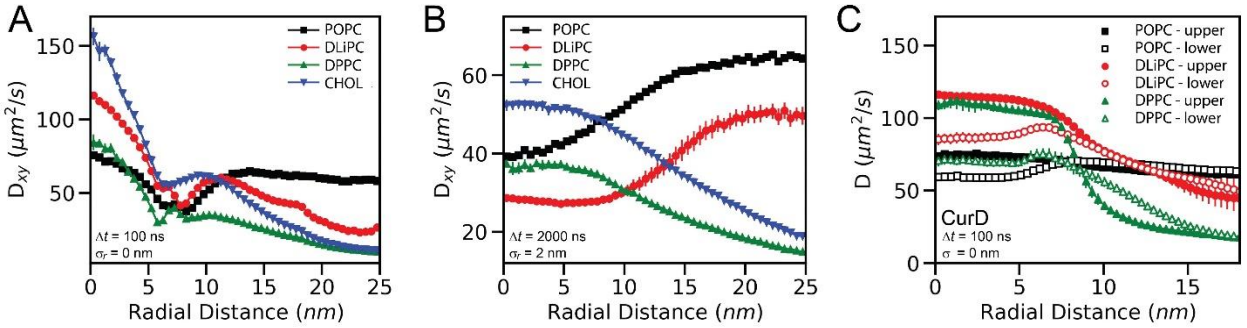

Figure 7:
The single-lipid step lengths from CG molecular dynamics simulations were analyzed to mimic the experimental analysis conditions for phase-separated and pure POPC compositions by calculating the diffusion rate through the XY-plane (D_{xy}). Compared to the experimental capabilities, molecular dynamics simulations provided a more frequent observation and greater certainty of the lipid locations over a smaller membrane bud. (A) When MSD analysis included Δt = 100 ns and no artificially added localization uncertainty (σ_r = 0), diffusion was faster on the curved membrane for all lipid types, consistent with the L_d phase sorting to the curvature. (B) But with analysis conditions that mimic the experimental conditions and incorporate greater spatial averaging (Δt = 2 μs; σ_r = 2 nm), then D_{xy} showed a lipid-type dependencies.

Here, the L_d-partitioning DLiPC and POPC show great qualitative diffusion similarities to the L_d-partitioning DPPE-TR observed experimentally (Fig. 6). (C) Molecular dynamics results were additionally subjected to a diffusion analysis with geodesic distance-based algorithms (CurD) to reveal the in-membrane diffusion separate from any projection effects. Here, the consistent curvature of the membrane bud had uniform diffusion rate without projection effects.

The CG simulations were also analyzed with single-lipid tracking analogously to how the experimental data was analyzed. CG simulations enable analysis with sub-microsecond Δt and with no localization imprecision (σ_r). When analyzed with Δt = 100 ns, the POPC lipids displayed minimal difference in diffusion on the hemispherical bud versus the planar bilayer (*i.e.,* $r < 3$ nm versus $r > 13$ nm), which shows that diffusion rates are unchanged by curvature in the absence of phase separation (Fig. 7A). The lower D_{xy} for the POPC lipids at r = 8 nm is attributed to the effects of projecting the 3D lipid locations into the XY-plane while motion along the Z-axis was not incorporated. However, upon the incorporation of a phase-separated lipid mixtures, all lipid types experienced faster diffusion on the membrane bud with Δt = 100 ns, correlated with the curvature-sorted L_d phase. The curvature-associated L_d phase provided a lower effective membrane viscosity such that all lipids in the phase-separated membrane diffused faster on the bud.

Analysis of the CG simulations was also performed with conditions mimicking those achieved experimentally (Fig. 7B). These computationally feasible, 5-nm bud CG simulations were analyzed with larger σ_r and Δt values so that similar spatial and temporal blurring was incorporated into both the CG and experimental data. To make the 5-nm CG buds mimic the 50-nm experimental buds, the CG lipid locations were blurred with σ_r applied at 10% of the experimental conditions, 2 nm and 20 nm, respectively. The Δt used for the mimicking CG analysis was 0.1% of that used experimentally, 2 μs and 2 ms, respectively, to account for the quadratic dependence of the lag time with the expected step length and the 10x faster diffusion observed in CG simulations versus experimental measurements (49). These analysis conditions resulted in consistent ratios of the localization uncertainty and mean step length to the curvature radius for both the CG simulations and experimental conditions. Additionally, the D_{xy} results presented from CG simulations were corrected with Eq. 6, as done experimentally.

When analyzing the POPC diffusion with longer time steps (Δt = 2 μs) and incorporating a localization uncertainty (σ_r = 2 nm) to mimic the spatial blurring observed experimentally, D_{xy} versus r for CG POPC closely resembles experimental results for nanoscale buds in quasi-single component supported lipid bilayers (Figs. 6A and 7B) with the changes in D_{xy} dominated by geometrical projection effects (Fig. 7C) (37, 45). With Δt = 2 μs and σ_r = 2 nm, the diffusion of CG DLiPC resembles that of the CG POPC and experimental DPPE-Texas Red results. But the DPPC and cholesterol diffusion shows significant increase in D_{xy} on the bud versus the surrounding planar membrane. This result further supports the observation of curvature-phase coupling and motivates the incorporation of an order-preferring fluorescent lipid in future experimental studies.

CG simulations provide the full 3D trajectory of each lipid, which enables resolving leaflet differences and removing the influence projecting lipids onto an imaging plane *via* the use of a geodesic distance-based analysis of the CG simulations (50). While the nuances of lipid diffusivity in spatially varying mean and Gaussian curvature are the focus of an upcoming manuscript, here we present the key results of the geodesic distance-based analysis, named *CurD*. To gain insight into the detailed lipid dynamics, the averaging effect of measurement time was mitigated by extracting the diffusion

coefficients for displacements Δt = 1 ns (Fig. S8C) and Δt = 100 ns (Fig. 7C). Both leaflets provided faster diffusion on the bud for phase-separated membranes. However, the use of geodesic distances demonstrated that the experimentally apparent slowing of lipids at 7 nm from the bud center is indeed due to the 2D projection of the 3D trajectories rather than a reflection of effective local membrane viscosity changes. Furthermore, it was revealed that the observed increase in lipid mobility correlated with the mean curvature. For a given lipid type, diffusion rates in the planar membrane region converged to a single value across both leaflets. Hydrodynamics dictates that the effective viscosity in a single phase should be the same for all lipid types (51). Here, the ratio of diffusion for DLiPC and DPPC lipids was closer to 0.5, which matched the ratio of diffusion coefficients in Martini simulations of planar phase separating systems (52). This finding is in agreement with the observation that the lipid phases propagated along the flat membrane and spanned the simulation box.

Discussion

This study provides a quantitative analysis of the phase–curvature coupling in membranes with shapes that are reminiscent of nanoscopic endocytic pits and viral buds. The membrane composition, temperature, and curvature were varied for experimental and simulated membranes. The phase–curvature coupling was revealed by the lateral heterogeneity in both the local density and the diffusion rates of disorder-preferring lipids by both experimental and computational methods. The curvature influenced the lipids more under conditions that provided a longer tie-line separating the coexisting phases, *i.e.*, lower temperature and less cholesterol. This may be explained by the correlation that the more ordered the surrounding phase, the higher its bending modulus. Thus, in mixtures where the ordered phase has low concentration of DiPhyPC, the energetic penalty for placing the ordered phase in the curved regions is high, leading to a more significant curvature-regulated sorting of the lipid phases.

The effects of curvature were still present in lipid mixtures when no phase separation was observed on the planar membrane, which suggests that the curvature was able to induce a phase separation and demonstrates the strength of our techniques to reveal nanoscopic lipid phases. This is consistent with a curvature-induced phase separation and that T_{mix} is dependent on the membrane shape. While pushing the limits of experimental and computational feasibility, these diverse methods provided broad agreement to provide cross-validation between the four complementary approaches employed. These results suggest that the dynamic curvature and composition of native biological membranes may couple to drive complex membrane processes in membrane signaling, shape changes, and pathophysiology.

Membrane brightness at curvature sites

The 1:1:2 SLBs phase sorting result indicated that the experimental ratio of P_C/P_F was greater than one for all values of P_F (Figs. 3 and S4); the disorder-preferring fluorescent lipid density was higher on curved membranes. The sorting was presumably due to the differences in the phase bending rigidity because the leaflets seemed to maintain phase registration, and we do not anticipate that the molecular shape (*e.g.*, the lipid packing parameter) of the fluorescent lipid was sufficient to induce significant single-molecule, phase-independent sorting (18, 25, 53). This is further supported by our observation

that quasi-one component membranes of POPC were not able to induce a curvature-dependent sorting of fluorescent lipids experimentally or alter the POPC density in CG simulations (Fig. 5F) (37).

Diffusion reveals the coupling of phases and curvature

The ratio of diffusion on curved versus flat membranes (D_C/D_F) was larger when phase separation was present (Fig. 6). Quasi-one component L_d membranes of DiPhyPC displayed no significant difference between D_C and D_F whereas mixtures of DiPhyPC, DPPC, and cholesterol displayed faster diffusion at curved surfaces regardless of if phase separation was observed on the planar membrane. This result is consistent with sorting studies where P_C/P_F values were above 1 for all P_F (Fig. 3C) and the CG simulations (Figs. 7 and S8). We hypothesize that this demonstrates the capability of curvature to induce phase separation that was not present on flat membranes by effectively increasing the local T_{mix}.

We did not observe a difference in the diffusion ratio D_C/D_F for membranes of varying surrounding phases, which was likely due to the intrinsic noise in the determination of the membrane phase surrounding each membrane bud. These diffusion studies were practically limited in the number of membrane buds able to be measured, the uncertainty of the phase at 400 nm away from each bud, and the single-lipid diffusion rates measured at each radial distance.

Curvature-seeded phase separation propagates onto the surrounding flat membrane

A subtle but consistent decrease in D_{xy} was observed on the flat membrane propagating away from the engineered curvature sites (Fig. 6B). This demonstrates that the effective membrane viscosity and the composition of the flat membrane varied with distance from the nanoparticle as if the curvature seeded a phase separation that propagated onto the surrounding flat membrane. This phenomenon was also observed in continuum and CG simulations of phase separation with the L_d phase more likely to be present on the flat membrane that is near the curvature versus far from the curvature. (Figs. 4 and 5). This seeding effect may prove to provide a longer-rate attraction of membrane components to the curvature sites. If the curvature sites can seed a phase separation and an extended gradient of the curvature-preferring phase onto the surrounding planar membrane, then the curvature site may more affectively recruit membrane-bound molecules into the membrane bud for selective endocytosis and trafficking.

Conclusions

Nanoscale membrane curvature was engineered in phase-separated supported lipid bilayers. The sorting and dynamics of lipids were measured to reveal the curvature-induced phase separation and the phase–curvature coupling at physiological length scales. The fluorescence intensity ratio of curvature versus surrounding planar bilayer from diffraction-limited images show the L_d-preferring lipids sorted to the engineered curvature. The single-lipid diffusion rates were measured versus the lateral distance away from the center of curvature to further support the curvature-induced sorting of disordered lipids. Unlike quasi-one component liquid DiPhyPC or POPC bilayers, SLBs with ternary mixtures of lipids showed a faster diffusion on the curved versus flat membranes. The effects of curvature on lipid diffusion and sorting were more pronounced under conditions in which the phase-separating tie-lines were longer, including lower temperatures and less cholesterol, and when the local

surrounding planar membrane was more ordered. These results indicate that the strong preference of disorder-preferring lipids to membranes curved at physiological scales.

These results demonstrate that the interplay between lipid phases and membrane shape may contribute to the cellular needs for lateral sorting on the membrane. Whereas single-molecule sorting to membrane buds may be too weak for a significant change in the membrane composition due to the curvature, the collective behavior of the lipids through phase separation may induce substantial changes to the membrane composition and behavior. For example, the sorting of lipid phases relative to membrane curvature would presumably both induce changes to the local membrane protein composition and affect further membrane shape changes, such as by altering the local membrane bending stiffness and leaflet asymmetry. In symmetric model membranes, the L_d phase is concentrated on more curved membranes presumably to the lower bending stiffness of the L_d phase relative to the L_o phase. But live cell membranes frequently have membrane buds correlated with L_o phases. This difference may come from the leaflet asymmetry in live cells which induces a phase-dependent intrinsic curvature, *i.e.*, the L_o phase may have an energy minimum in a curved geometry while the L_d phase may prefer to be planar. The interplay between lipid phase and membrane shape is potentially of fundamental importance for essential plasma membrane and organelle functions. The experimental and computational results presented here reveal ability and limitations of <100 nm membrane buds to induce and sort lipid phases.

Methods

This manuscript incorporates a diverse collection of experimental and computational methods that are detailed in the Supporting Information. The formation of GUVs, SLBs, and nanoengineered substrates are detailed in Supplemental Material §S.1 and §S.2. To maintain the large-scale phase separation in the SLBs like as observed on the GUVs, required precise temperature control of the sample and substrate was required during SLB formation (§S.3). The diffraction-limited imaging (§S.4) and single-molecule localizations (§S.5) occurred with precise sample temperature control (§S.6). Data analysis included spatial mapping of the lipid phases (§S.7), membrane curvature (§S.8), single-particle tracking (§S.9), and diffusion coefficient calculations (§S.10). Considerations of the effects of the fluorophore (§S.11) and the substrate (§S.12) on the lipid dynamics are presented. Computational approaches include the continuum simulations with explicit phase-curvature coupling (§S.13) and coarse-grained molecular dynamics simulations (§S.14).

Supporting Information Appendix (SI)

This article contains supporting information describing the materials, methods, and experimental considerations for this manuscript. Two supplemental movies, eight supplemental movies, and one supplemental table are included. The supplemental movies are available in high resolution from Ref. (53).

Acknowledgements

The authors thank Aurelia R. Honerkamp-Smith for valuable discussions. CSC – IT Center of Science is acknowledged for computational resources. X.W. was supported by the Thomas C. Rumble

University graduate fellowship, Wayne State University Summer Dissertation Award, and the Richard Barber Interdisciplinary Research Program. M.J. was supported by an Academy of Finland postdoctoral researcher grant (Grant No. 338160) and the Emil Aaltonen Foundation. This material is based upon work supported by the National Science Foundation under Grant No. DMR1652316.

Author Contributions

X.W., M.J., B.F., and C.V.K. wrote the manuscript. X.W. and C.V.K. designed the experiments and performed the data analysis. X.W. performed the experiments. C.V.K. performed the continuum simulations. M.J. and B.F. performed the CG simulations.

Author Declaration

The authors declare no competing interest.

References

1. Pralle, A., P. Keller, E.-L. Florin, K. Simons, and J.K.H. Hörber. 2000. Sphingolipid–Cholesterol Rafts Diffuse as Small Entities in the Plasma Membrane of Mammalian Cells. *J Cell Biol*. 148:997–1008.

2. Simons, K., and E. Ikonen. 1997. Functional rafts in cell membranes. *Nature*. 387:569–572.

3. Honerkamp-Smith, A.R., P. Cicuta, M.D. Collins, S.L. Veatch, M. den Nijs, M. Schick, and S.L. Keller. 2008. Line tensions, correlation lengths, and critical exponents in lipid membranes near critical points. *Biophys. J.* 95:236–246.

4. Shaw, T.R., S. Ghosh, and S.L. Veatch. 2021. Critical Phenomena in Plasma Membrane Organization and Function. *Annu Rev Phys Chem*. 72:51–72.

5. Fessler, M.B., and J.S. Parks. 2011. Intracellular lipid flux and membrane microdomains as organizing principles in inflammatory cell signaling. *J. Immunol.* 187:1529–1535.

6. Hurley, J.H., E. Boura, L.-A. Carlson, and B. Rózycki. 2010. Membrane Budding. *Cell*. 143:875–887.

7. Simons, K., and D. Toomre. 2000. Lipid rafts and signal transduction. *Nat. Rev. Mol. Cell Biol.* 1:31–39.

8. Waheed, A.A., and E.O. Freed. 2010. The Role of Lipids in Retrovirus Replication. *Viruses*. 2:1146–1180.

9. Mukherjee, S., and F.R. Maxfield. 2000. Role of membrane organization and membrane domains in endocytic lipid trafficking. *Traffic*. 1:203–211.

10. Parton, R.G., and K. Simons. 2007. The multiple faces of caveolae. *Nat. Rev. Mol. Cell Biol.* 8:185–194.

11. Parton, R.G., M.A. Del Pozo, S. Vassilopoulos, I.R. Nabi, S. Le Lay, R. Lundmark, A.K. Kenworthy, A. Camus, C.M. Blouin, W.C. Sessa, and C. Lamaze. 2020. Caveolae: The FAQs. *Traffic*. 21:181–185.

12. Veatch, S.L., and S.L. Keller. 2002. Organization in lipid membranes containing cholesterol. *Phys. Rev. Lett.* 89:268101.

13. Veatch, S.L., and S.L. Keller. 2005. Seeing spots: Complex phase behavior in simple membranes. *Biochimica et Biophysica Acta (BBA) - Molecular Cell Research*. 1746:172–185.

14. Roux, A., D. Cuvelier, P. Nassoy, J. Prost, P. Bassereau, and B. Goud. 2005. Role of curvature and phase transition in lipid sorting and fission of membrane tubules. *EMBO J.* 24:1537–1545.

15. Sorre, B., A. Callan-Jones, J.-B. Manneville, P. Nassoy, J.-F. Joanny, J. Prost, B. Goud, and P. Bassereau. 2009. Curvature-driven lipid sorting needs proximity to a demixing point and is aided by proteins. *Proc Natl Acad Sci U S A*. 106:5622–5626.

16. Tian, A., and T. Baumgart. 2009. Sorting of Lipids and Proteins in Membrane Curvature Gradients. *Biophys. J.* 96:2676–2688.

17. Heinrich, M., A. Tian, C. Esposito, and T. Baumgart. 2010. Dynamic sorting of lipids and proteins in membrane tubes with a moving phase boundary. *Proceedings of the National Academy of Sciences*. 107:7208–7213.

18. Kamal, M.M., D. Mills, M. Grzybek, and J. Howard. 2009. Measurement of the membrane curvature preference of phospholipids reveals only weak coupling between lipid shape and leaflet curvature. *PNAS*. 106:22245–22250.

19. Ogunyankin, M.O., D.L. Huber, D.Y. Sasaki, and M.L. Longo. 2013. Nanoscale patterning of membrane-bound proteins formed through curvature-induced partitioning of phase-specific receptor lipids. *Langmuir*. 29:6109–6115.

20. Yoon, T.-Y., C. Jeong, S.-W. Lee, J.H. Kim, M.C. Choi, S.-J. Kim, M.W. Kim, and S.-D. Lee. 2006. Topographic control of lipid-raft reconstitution in model membranes. *Nat Mater*. 5:281–285.

21. Parthasarathy, R., C. Yu, and J.T. Groves. 2006. Curvature-modulated phase separation in lipid bilayer membranes. *Langmuir*. 22:5095–5099.

22. Baumgart, T., S. Das, W.W. Webb, and J.T. Jenkins. 2005. Membrane Elasticity in Giant Vesicles with Fluid Phase Coexistence. *Biophys J*. 89:1067–1080.

23. Waheed, A.A., and E.O. Freed. 2009. Lipids and membrane microdomains in HIV-1 replication. *Virus Res.* 143:162–176.

24. Lipowsky, R. 1993. Domain-induced budding of fluid membranes. *Biophys J*. 64:1133–1138.

25. Cooke, I.R., and M. Deserno. 2006. Coupling between Lipid Shape and Membrane Curvature. *Biophys. J.* 91:487–495.

26. Cheney, P.P., A.W. Weisgerber, A.M. Feuerbach, and M.K. Knowles. 2017. Single Lipid Molecule Dynamics on Supported Lipid Bilayers with Membrane Curvature. *Membranes (Basel)*. 7.

27. Larsen, J.B., M.B. Jensen, V.K. Bhatia, S.L. Pedersen, T. Bjørnholm, L. Iversen, M. Uline, I. Szleifer, K.J. Jensen, N.S. Hatzakis, and D. Stamou. 2015. Membrane curvature enables N-Ras lipid anchor sorting to liquid-ordered membrane phases. *Nat. Chem. Biol.* 11:192–194.

28. Dietrich, C., L.A. Bagatolli, Z.N. Volovyk, N.L. Thompson, M. Levi, K. Jacobson, and E. Gratton. 2001. Lipid rafts reconstituted in model membranes. *Biophys. J.* 80:1417–1428.

29. Scherfeld, D., N. Kahya, and P. Schwille. 2003. Lipid dynamics and domain formation in model membranes composed of ternary mixtures of unsaturated and saturated phosphatidylcholines and cholesterol. *Biophys J*. 85:3758–3768.

30. Filippov, A., G. Orädd, and G. Lindblom. 2004. Lipid lateral diffusion in ordered and disordered phases in raft mixtures. *Biophys J*. 86:891–896.

31. Chiantia, S., J. Ries, N. Kahya, and P. Schwille. 2006. Combined AFM and two-focus SFCS study of raft-exhibiting model membranes. *Chemphyschem*. 7:2409–2418.

32. Ge, Y., J. Gao, R. Jordan, and C. Naumann. 2018. Changes in Cholesterol Level Alter Integrin Sequestration in Raft-Mimicking Lipid Mixtures. *Biophys. J.* 114:158–167.

33. Wu, H.-M., Y.-H. Lin, T.-C. Yen, and C.-L. Hsieh. 2016. Nanoscopic substructures of raft-mimetic liquid-ordered membrane domains revealed by high-speed single-particle tracking. *Scientific Reports*. 6:20542.

34. Woodward, X., and C.V. Kelly. 2020. Single-lipid dynamics in phase-separated supported lipid bilayers. *Chem Phys Lipids*. 233:104991.

35. Gov, N.S. 2006. Diffusion in curved fluid membranes. *Phys Rev E Stat Nonlin Soft Matter Phys*. 73:041918.

36. Domanov, Y.A., S. Aimon, G.E.S. Toombes, M. Renner, F. Quemeneur, A. Triller, M.S. Turner, and P. Bassereau. 2011. Mobility in geometrically confined membranes. *Proc. Natl. Acad. Sci. U.S.A.* 108:12605–12610.

37. Woodward, X., E.E. Stimpson, and C.V. Kelly. 2018. Single-lipid tracking on nanoscale membrane buds: The effects of curvature on lipid diffusion and sorting. *Biochimica et Biophysica Acta (BBA) - Biomembranes*. 1860:2064-2075.

38. Yesylevskyy, S.O., T. Rivel, and C. Ramseyer. 2017. The influence of curvature on the properties of the plasma membrane. Insights from atomistic molecular dynamics simulations. *Sci Rep*. 7:16078.

39. Veatch, S.L., and S.L. Keller. 2003. A Closer Look at the Canonical 'Raft Mixture' in Model Membrane Studies. *Biophys. J.* 84:725–726.

40. Gunderson, R.S., and A.R. Honerkamp-Smith. 2018. Liquid-liquid phase transition temperatures increase when lipid bilayers are supported on glass. *Biochimica et Biophysica Acta (BBA) - Biomembranes*. 1860:1965–1971.

41. Kabbani, A.M., and C.V. Kelly. 2017. The Detection of Nanoscale Membrane Bending with Polarized Localization Microscopy. *Biophys. J.* 113:1782–1794.

42. Boyd, K.J., and E.R. May. 2018. BUMPy: A Model-Independent Tool for Constructing Lipid Bilayers of Varying Curvature and Composition. *J Chem Theory Comput*. 14:6642–6652.

43. Marrink, S.J., H.J. Risselada, S. Yefimov, D.P. Tieleman, and A.H. de Vries. 2007. The MARTINI force field: Coarse grained model for biomolecular simulations. *J. Phys. Chem. B*. 111:7812–7824.

44. Kabbani, A.M., K. Raghunathan, W.I. Lencer, A.K. Kenworthy, and C.V. Kelly. 2020. Structured clustering of the glycosphingolipid GM1 is required for membrane curvature induced by cholera toxin. *Proc. Natl. Acad. Sci. U.S.A.* 117:14978–14986.

45. Kabbani, A.M., X. Woodward, and C.V. Kelly. 2017. Revealing the Effects of Nanoscale Membrane Curvature on Lipid Mobility. *Membranes (Basel)*. 7.

46. Bag, N., D.H.X. Yap, and T. Wohland. 2014. Temperature dependence of diffusion in model and live cell membranes characterized by imaging fluorescence correlation spectroscopy. *Biochim. Biophys. Acta*. 1838:802–813.

47. Sengupta, P., A. Hammond, D. Holowka, and B. Baird. 2008. Structural Determinants for Partitioning of Lipids and Proteins Between Coexisting Fluid Phases in Giant Plasma Membrane Vesicles. *Biochim. Biophys. Acta*. 1778:20–32.

48. Tamm, L.K. 1988. Lateral diffusion and fluorescence microscope studies on a monoclonal antibody specifically bound to supported phospholipid bilayers. *Biochemistry*. 27:1450–1457.

49. Marrink, S.J., and D.P. Tieleman. 2013. Perspective on the Martini model. *Chem Soc Rev*. 42:6801–6822.

50. Fábián, B., and M. Javanainen. 2021. CurD: A Tool for Diffusion Analyses on Curved Membranes. *ChemRxiv*. Available at https://chemrxiv.org/engage/chemrxiv/article-details/6162d1ad8b620d83564a965d

51. Lindblom, G., G. Orädd, and A. Filippov. 2006. Lipid lateral diffusion in bilayers with phosphatidylcholine, sphingomyelin and cholesterol: An NMR study of dynamics and lateral phase separation. *Chemistry and Physics of Lipids*. 141:179–184.

52. Thallmair, S., M. Javanainen, B. Fábián, H. Martinez-Seara, and S.J. Marrink. 2021. Nonconverged Constraints Cause Artificial Temperature Gradients in Lipid Bilayer Simulations. *J Phys Chem B*. 125:9537–9546.

53. Callan-Jones, A., B. Sorre, and P. Bassereau. 2011. Curvature-Driven Lipid Sorting in Biomembranes. *Cold Spring Harb Perspect Biol*. 3.

54. Jaqaman, K., D. Loerke, M. Mettlen, H. Kuwata, S. Grinstein, S.L. Schmid, and G. Danuser. 2008. Robust single-particle tracking in live-cell time-lapse sequences. *Nat. Methods*. 5:695–702.

55. Kabbani, A.M., and C.V. Kelly. 2017. Nanoscale Membrane Budding Induced by CTxB and Detected via Polarized Localization Microscopy. *Biophys. J.* 113:1795–1806.

56. Ovesný, M., P. Křížek, J. Borkovec, Z. Švindrych, and G.M. Hagen. 2014. ThunderSTORM: a comprehensive ImageJ plug-in for PALM and STORM data analysis and super-resolution imaging. *Bioinformatics*. btu202.

57. Lagerholm, B.C., D.M. Andrade, M.P. Clausen, and C. Eggeling. 2017. Convergence of lateral dynamic measurements in the plasma membrane of live cells from single particle tracking and STED-FCS. *J Phys D Appl Phys*. 50:063001.

58. Qian, H., M.P. Sheetz, and E.L. Elson. 1991. Single particle tracking. Analysis of diffusion and flow in two-dimensional systems. *Biophys J*. 60:910–921.

59. Berglund, A.J. 2010. Statistics of camera-based single-particle tracking. *Phys Rev E Stat Nonlin Soft Matter Phys*. 82:011917.

60. Mobarak, E., M. Javanainen, W. Kulig, A. Honigmann, E. Sezgin, N. Aho, C. Eggeling, T. Rog, and I. Vattulainen. 2018. How to minimize dye-induced perturbations while studying biomembrane structure and dynamics: PEG linkers as a rational alternative. *Biochim Biophys Acta Biomembr*. 1860:2436–2445.

61. Machán, R., and M. Hof. 2010. Lipid diffusion in planar membranes investigated by fluorescence correlation spectroscopy. *Biochim Biophys Acta*. 1798:1377–1391.

62. Kelly, C.V. 2022. Continuum-membrane-phase-curvature-simulation. GitHub. Available at https://github.com/CVKellyWSU/Continuum-membrane-phase-curvature-simulation

63. Sadeghi, S., M. Müller, and R.L.C. Vink. 2014. Raft formation in lipid bilayers coupled to curvature. *Biophys. J.* 107:1591–1600.

64. Rangamani, P. 2022. The many faces of membrane tension: Challenges across systems and scales. *Biochim Biophys Acta Biomembr*. 1864:183897.

65. Abraham, M.J., T. Murtola, R. Schulz, S. Páll, J.C. Smith, B. Hess, and E. Lindahl. 2015. GROMACS: High performance molecular simulations through multi-level parallelism from laptops to supercomputers. *SoftwareX*. 1–2:19–25.

66. Cino, E.A., and D.P. Tieleman. 2022. Curvature-based sorting of eight lipid types in asymmetric buckled plasma membrane models. *Biophys J*. 121:2060–2068.

67. Javanainen, M. 2020. Simulations of POPC membranes of various shapes. Zenedo. 4196842. Available at https://zenodo.org/record/4196842

68. Javanainen, M., and B. Fabian. 2021. Ternary lipid composition in a curved geometry. Zenedo. 4445375. Available at https://zenodo.org/record/4445375

69. Veatch, S.L., K. Gawrisch, and S.L. Keller. 2006. Closed-Loop Miscibility Gap and Quantitative Tie-Lines in Ternary Membranes Containing Diphytanoyl PC. *Biophys. J.* 90:4428–4436.

Supplemental Materials and Methods

S.1 GUV formation

The lipids 1,2-diphytanoyl-sn-glycero-3-phosphocholin (DiPhyPC), 1,2-dioleoyl-sn-glycero-3-phosphocholine (DOPC), 1,2-dipalmitoyl-sn-glycero-3-phosphocholine (DPPC), 1-palmitoyl-2-oleoyl-glycero-3-phosphocholine (POPC), and cholesterol (Avanti Polar Lipids) were used without further purification (Fig. 2). Fluorescent dihexadecanoylphosphoethanolamine 1,2-dipalmitoyl-sn-glycero-3-phosphoethanolamine-Texas Red (DPPE-Texas Red, Life Technologies) was included at 0.1 mol\% for labeling for all membranes with DiPhyPC or POPC.\ 1-palmitoyl-2- (dipyrrometheneboron difluoride) undecanoyl-sn-glycero-3- phosphocholine (TopFluor-PC; Avanti Polar lipids) was included at 0.2 mol% in membranes with DOPC. Milli-Q water with a resistivity of 18 mΩ was used in all buffers. All other chemicals were purchased from Sigma Aldrich.

GUVs were created by electroformation, as described previously (54). Briefly, lipids were combined in chloroform and dried onto conducting indium tin oxide-coated glass plates. A trimmed silicon sheet was added between the plates to form the incubation chamber. The chamber was filled with a 200 mM sucrose solution and subjected to an AC signal with 3 V_{rms} at 10 Hz for 1 hr at 55 °C. The GUV solution had 13 mg of lipids per mL after electroformation. GUVs were stored at 55 °C and used within 2 days.

S.2 Sample dish preparation

Glass-bottom dishes (MatTek Corp.) were initially rinsed with ethanol, blown dry by a nitrogen stream, then placed in air plasma (Harrick Plasma) for 10 s to create a hydrophilic surface. 20 µL of 5 mM $CaCl_2$ was spun on a glass substrate at 100 rpm. 50-nm radius fluorescent nanoparticles that were excited at 405 nm (Fluoro-Max; Fisher Scientific) were used for generating curvature, and multicolored nanoparticles (TetraSpeck, ThermoFisher Scientific Technologies) were used as stage drift correction fiducial marks. The nanoparticle-containing solutions were evaporated from the coverslips by a hot plate at 35 °C for 5 min. The dishes were then chilled to room temperature prior to GUV deposition. The phase and temperature varying experiments performed here were too difficult to also incorporate varying nanoparticle sizes as was performed previously on single-phase SLBs (37).

S.3 Supported lipid bilayer formation

SLBs with engineered curvature were created by GUV fusion over nanoparticles on microscopy coverslips, similar to as done previously (26, 37, 41, 55). However, new methods for preserving the large-scale phase separation from GUVs in solution to SLB patches on the coverslip were developed here. The GUV solution was placed in the refrigerator at 4 °C for 2 minutes to assist the macro-domain formation. 5 µL of the chilled GUV solution was applied to the room temperature glass bottom dishes with nanoparticles. 50 µL of 4 °C Milli-Q water was added to encourage the GUVs to sink to the cover glass. The dish was chilled to 4 °C for 15 min before gently rinsing with 5 mL of 4 °C, 200 mM sucrose.

S.4 Imaging procedure

The optical setup included an inverted IX83 microscope with a 100x, 1.49 NA objective (Olympus), a 2x emission path magnification (OptoSplit, Cairn Research), and an iXon 897-Ultra EMCCD

camera (Andor Technology), as described previously (37, 44, 55, 55). A Hg lamp with an excitation filter (BrightLine single-band filters, Semrock) provided illumination for diffraction-limited images (*i.e.*, Fig. 2A). CUBE diode lasers with wavelengths of 405 and 488 nm (Coherent) and a 561 nm Sapphire laser (Coherent) were used for single-molecule localization microscopy. The excitation light passed through a clean-up filter (zet405/488/561/647x, Chroma Technology), encountered a quad-band dichroic mirror (zt405/488/561/647rpc, Chroma Technology), and reflected into the objective. The emission was isolated via emission filters (BrightLine single-band filters, Semrock) and a 4-band notch filter (zet405/488/561/640m, Chroma Technology). The SOLIS imaging software (Andor Technology) was used to acquire images with 128 pixels x 128 pixels region of interest in the kinetic mode and an EM gain of 150. The images for single-molecule localization were acquired at 537 Hz. Typically, 20,000 frames were combined to create reconstructed, super-resolution images or analyzed for single-particle tracking.

The degree of lipid sorting with curvature was quantified by measuring the fluorescence intensity difference between the engineered curvature and the surrounding planar membrane via diffraction-limited epifluorescence imaging. The membrane intensity in diffraction-limited images represents the fluorophore concentration with 200 nm resolution. Diffraction-limited imaging requires two orders of magnitude less illumination intensity than super-resolution imaging. Also, our super-resolution methods show only a few fluorophores per frame and required >20,000 frames to study the diffusion or to reconstruct images. Each curvature site of a POPC membrane provided between 1-30x higher density of DPPE-Texas Red localizations than the planar bilayer, which is of significantly greater variation between buds than observed via diffraction-limited imaging, which was 1 to 2.5x. Therefore diffraction-limited images were used for phase-sorting studies.

S.5 Single-fluorophore localization

The movies with optically isolated fluorescent lipids were analyzed by the Fiji plug-in ThunderSTORM, which fit every single-fluorophore image with a 2D Gaussian function to export its location, intensity, fit width, and fit certainty (56). Only the localizations with intensity > 100 photons, Gaussian fit width > 15 nm, and location uncertainty < 45 nm were kept for further analysis. The ThunderSTORM-reported fluorophore uncertainty (σ_r) was 24 ± 1 nm. The stage drift during imaging was corrected by analyzing the motion of the multicolored nanoparticles through built-in ThunderSTORM fiducial tracking, which was separate from the nanoparticles used to engineering membrane curvature.

Super-resolution images reconstructed from single-fluorophore localizations contained aggregates of DPPE-Texas Red in the DiPhyPC-containing membranes. The clusters of these dense, aggregate localizations were 63 ± 17 nm radius and showed confinement in lipid diffusion. DiPhyPC contains phytanoyl acyl tails that are highly disordered and have reduced photo-oxidization compared to unsaturated lipids. Photo-stability is especially appreciated in experiments that rely on phase separations that are sensitive to the membrane composition.

Aggregates were identified and removed by custom algorithms that were studied extensively previously (37). Aggregates were removed via binning all localizations into voxels of space and acquisition time and culling based on a threshold localization rate. When the number of localizations in a voxel exceeded the localization density threshold (ρ_{th}), that region of the sample was deemed to be an aggregate, and all localizations within that XY-region were excluded from subsequent analysis. Further, all localizations associated with trajectories that lasted more than 32 steps were culled. The value of ρ

was varied such that between 0 and 80 percentiles of the total localizations were culled. For each ρ_{th}, a simulated membrane was generated with an evenly distributed localizations except the removed region. A spatial correlation function was calculated for both the experimental and simulated membrane and the remaining localizations according to

$$g(r) = \frac{\left\langle \mathrm{FFT}^{-1}\left(|\mathrm{FFT}(I(\mathbf{r}))|^2\right)\right\rangle_\theta}{\rho^2}. \quad \text{(S1)}$$

$I(\boldsymbol{r})$ represents the two-dimensional localization histogram, and ρ is the average localization density. The average number of localizations per cluster can be calculated by comparing the spatial correlation of the two.

$$N = \int \left(\frac{g_{\mathrm{exp}}}{g_{\mathrm{sim}}} - 1\right) r\mathrm{d}r. \quad \text{(S2)}$$

N was calculated for all localization data sets with varying ρ_{th}. The minimum ρ_{th} for which $N \leq 3$ was used for the diffusion studies.

S.6 Membrane temperature control

A Peltier temperature control dish holder (QE-1HC, Warner Instruments) was used with a custom, insulated dish cover with a thermocouple mount. Once the dish cover is placed on the sample dish, the thermocouple was <0.5 mm above the center of the glass coverslip. The temperature was actively controlled via a custom LabVIEW program. Also, the dishes were never heated above 45 °C to protect the microscope objective. When changing temperature, the temperature was changed at 0.5 °C /min and remained at the set temperature for 30 min before imaging. The Peltier dish holder was initially set to 10 °C before inserting a membrane sample. The Peltier temperature was set to be at 10 °C, 30 °C, and 45 °C resulted in the thermocouple measuring a temperature of (17 ± 3) °C, (27 ± 1) °C, and (37 ± 1) °C, respectively.

S.7 Lipid phase identification

The 2D projected image of a homogeneous membrane yields an increased brightness at the location of membrane curvature compared to the surrounding planar membrane due to the increase in the projected membrane area. Coincident nanoparticles confirmed the membrane curvature in the appropriate color channel. A single 2D Gaussian fit was used to find the center of membrane curvature in the membrane color channel.

The lipid phase was quantified by the partition coefficient of the fluorescent lipids. Both DPPE-Texas Red and TopFluor-PC are L_d preferring lipids (57, 58), and the higher local concentration was interpreted as a greater degree of disorder in the acyl tails. The intensity of the curved membrane (I_C) is defined as the average intensity of the nine pixels within 170 nm from the center of curvature, and the intensity surrounding the curvature (I_F) is defined as the average intensity of the pixels 400 ± 56 nm away from curvature from diffraction-limited images (Fig. S3). The increased membrane brightness due to the membrane topography was determined from homogeneous POPC membranes and analytical

models of the membrane shape, which provide the expected membrane curvature intensity increase due to the increased membrane area in the XY-projection, I_C^{POPC}/I_F^{POPC} = 1.23. The average membrane intensity (<*I*>) is defined as the midpoint of the mean L_d phase intensity (I_d) and mean L_o phase intensity (I_o) from each planar SLB patch; <*I*> = (I_d + I_o)/2. This definition of <I> accounts for individual fields of view that happened to contain more of one phase than the other. When no phase separation was present on the flat membrane, <*I*> = I_F. The lipid phase on the flat membrane surrounding the curvature (P_F) and the phase of the curvature (P_C) according to

$$P_F = I_F/\langle I \rangle, \tag{S3}$$

$$P_C = \frac{I_C}{\langle I \rangle}\frac{I_F^{POPC}}{I_C^{POPC}}. \tag{S4}$$

This method of determining the lipid phase from fluorescence images accounts for sample-to-sample variation in fluorophore concentrations and temporal changes caused by fluorescence bleaching. The phase surrounding the membrane curvature was determined *r* = 400 nm (Fig. S3) with P_F < 0.9 indicating the L_o phase and P_F > 1.1 indicating the L_d phase. Homogeneous, multicomponent membrane at a temperature above T_{mix} is recognized as a single fluid-phase membrane. This classification was used for sorting the curvature sites based on their surrounding lipid phase for diffusion analysis (Figs. 3 and 6). The P_F values varied depending on *r*, which resulted in an uncertainty of the SLB phase and yielded no difference in the DPPE-Texas Red diffusion at *r* = 600 nm. A more precise analysis of the effects of P_F is shown in with diffraction-limited imaging when the classification of the phases was not necessary, and the value of P_F surrounding each nanoparticle could be directly reported (Fig. 3). However, the diffusion analysis required combining the data from multiple nanoparticles to yield statistically meaningful results. A more robust analysis of the phase-dependent diffusion of fluorescent lipids on planar SLBs was provided previously (37).

S.8 Super-resolved curvature identification and aggregate removing method

Reconstructed super-resolution images of single lipids revealed increased localization density at the sites of membrane curvature. Curvature was confirmed by the colocalization of fluorescent nanoparticles and lipid accumulations in the complementary color channels. The local density increase in single-lipid localizations was fitted to a 2D Gaussian function to find the exact curvature center for the super-resolution images and single-particle tracking analysis.

DiPhyPC-containing SLBs yield aggregates of DPPE-Texas Red (37). Aggregates were apparent via a high fluorophore localization density in the absence of nanoparticles. Comparisons between membrane curvature events and fluorophore aggregates were made via the size of the cluster of localizations, the local single-lipid diffusion rate, localization density, localization rate, and the proximity to the nanoparticles. Aggregates were removed via localization density and long trajectory culling, as described in the Supplemental Material and previously (34). Briefly, all localizations that were not associated with membrane curvature were grouped based on their 2D location and acquisition time into 3D voxels. When the number of localizations in a voxel exceeded the localization density threshold (ρ_{th}), that region of the sample was deemed to be an aggregate and all localizations within that XY-region

were excluded from subsequent analysis. Further, all localizations associated with trajectories that lasted more than 32 steps were culled.

S.9 Single-particle tracking

The single-lipid localizations were linked via u-track with a maximum step length of 400 nm (54). The average trajectory length of the aggregate-removed localizations was 6 ± 4 steps. Only the single-lipid steps between adjacent frames (v) were used in our analysis while being versus their lateral radial distance away from the center of curvature (*r*) and fit to a 2D Rayleigh distribution (*r*) (34, 55),

$$R(v) = \frac{v}{2D_{\text{fit}}\Delta t} \exp\left(-\frac{v^2}{4D_{\text{fit}}\Delta t}\right). \quad \text{(S5)}$$

Fitting of Eq. S5 incorporates the time between sequential frames (Δt) and yields a fit diffusion coefficient (D_{fit}). D_{fit} was corrected for imaging blur created by the single-frame exposure time (t_{exp}) and localization uncertainty (σ_r) (59) according to

$$D_{xy} = \frac{D_{\text{fit}} - \frac{\sigma_r^2}{2\Delta t}}{1 - \frac{t_{\text{exp}}}{3\Delta t}}. \quad \text{(S6)}$$

When Eq. S6 was applied to CG simulations with a $\sigma_r > 0$ applied to mimic the experimental conditions, $t_{exp} = 0$ because the instantaneous lipid COM was calculated without blurring over an exposure time.

S.10 Monte Carlo fitting of diffusion

The measured lateral diffusion rates (D_{xy}) vs. radial distance from the nanoparticle center (*r*) includes contributions from both the effects of local curvature on the lipid mobility and the 3D membrane shape projected into the XY-imaging plane. To extract the separate contribution of these two effects, Monte Carlo simulations were performed (34, 55). Individual lipids were simulated diffusing on a curved surface that estimates the shape of the SLB draped over the nanoparticle on cover glass (Fig. S5). First, available locations for the lipid on the membrane were created at a density of 4 nm^2. Second, a single-lipid trajectory was calculated by allowing the lipid to randomly step to one of the 110 ± 10 points within 3 nm of its current location with an average step length of 2 nm. These step lengths were significantly smaller than the surface's radius of curvature. A duration of time was associated to each single lipid step (Δt_1) to set a local effective diffusion coefficient. For example, when $\Delta t_1 = 0.45$ μs, then a local diffusion coefficient in the membrane of 2.5 $\mu m^2/s$ was simulated. This local diffusion coefficient represents the in-plane diffusion for the membrane, regardless of the membrane's local orientation relative to the XY-plane. Varying curvature-induced changes to lipid diffusion were simulated by mimicking a different local D, *i.e.* spatially dependent Δt_1 values. The simplifying assumption was made to reduce fitting parameters that all lipid diffusion on the planar membrane had one diffusion coefficient and all membrane with curvature had a second diffusion coefficient.

To connect these Monte Carlo simulations to the experimental data, trajectories were calculated until the cumulative time of 1.86 ms had elapsed, which is the frame rate of our experimental single-molecule localization and SPT. If a constant $\Delta t_1 = 0.45$ μs was used, then a single-lipid trajectory

included 413 steps. When Delta t_1 varied during the lipid trajectory, the number of simulated steps in a single trajectory varied. The random trajectories starting and ending locations on the membrane were

$$D_C = D_{xy}(r \leq 50 \text{ nm})/0.53, \quad \text{(S7)}$$

$$D_F = D_{xy}(400 \text{ nm} \leq r \leq 600 \text{ nm}). \quad \text{(S8)}$$

saved and analyzed as if they were sequential frames in an SPT experiment. Additionally, a 20 nm standard deviation Gaussian localization imprecision was applied. The single-lipid step lengths were projected into the XY-plane and analyzed vs. lateral radial distance from the curvature center across the sample were analyzed just as was done for the experimental data with *T*_{exp} = 0$. A matrix of Monte Carlo simulations was performed with varying Δt_1 for the planar membrane and Δt_1 for the curved membrane. This matrix of Monte Carlo results was fit to the experimentally acquired D_{xy} vs. *r* to extract the effective diffusion coefficient on the flat and planar membranes. The extensive, dense sampling of quasi-single-component membranes revealed a consistent geometrical effect of XY-projection on the observed D_{xy} vs. *r*. The simulations show that $D_{xy}(r \leq 50 \text{ nm})$ underestimates the in-membrane diffusion by a factor of 0.53 ± 0.10 due to the membrane tilt relative to the XY-plane for membranes wrapping the 50-nm radius nanoparticles. The single-fluorophore localizations could not feasibly be acquired densely for the curved, phase-separated membranes presented in this manuscript. Accordingly, the diffusion of the curved (D_C) and flat (D_F) membranes is approximated by

S.11 Effects of the fluorescent lipid

The lipid diffusion with nanoscale curvature varies with the fluorescence labeling strategy. For example, DPPE-Texas Red lipid diffusion in POPC bilayer in a curved membrane displayed a diffusion rate 40% of that of the flat membrane, $D_C/D_F = 0.4 \pm 0.1$. However, TopFluor-PC showed no difference in diffusion with membrane bending, $D_C/D_F = 1.0 \pm 0.2$ (37). DPPE-Texas Red was primarily used rather than TopFluor-PC throughout this manuscript because it was brighter, it could be used at lower concentrations, and it required less intense fluorescence illumination power. Moreover, tail-labeled fluorescent lipids perturb membrane more than head group-labeled fluorescent lipids as measured by transient binding versus free diffusion, which indicates the level of trapping interactions (60).

S.12 Effects of the substrate on lipid diffusion

The diffusion of individual lipids and phase domains in SLBs are affected by the substrate's close proximity to the bilayer's lower leaflet. This substrate proximity slows the diffusion of single lipids in SLB to 10-50% of the observed diffusion in vesicles or black lipid membranes (61). Similarly, the diffusion in the bilayer's top leaflet, distal from the substrate, is 1.1-1.3x faster than the single-lipid diffusion in the bottom, proximal leaflet (37). Whereas the substrate roughness and surface chemistry can greatly affect lipid diffusion, we have examined the SPT of fluorescent lipids in the leaflets separately to confirm that the nanoparticle vs. coverslip surface properties do not contribute to the D_C/D_F values reported in this manuscript (37).

S.13 Continuum simulations with explicit phase-curvature coupling

Custom Python code used to perform these simulations is freely available (62). Lipid phase separation and phases-curvature coupling was modeled with a Hamiltonian consisting of three parts: membrane height fluctuations via the Helfrich form; local compositional fluctuations via a fourth-order Landau expansion; and curvature-composition coupling (63, 64),

$$H = \int \left[\kappa \left(c - c_0 \right)^2 + \kappa_G K - \lambda + A_L \phi^2 + B_L \left(\nabla \phi \right)^2 + C_L \phi^4 - \gamma \phi |c| \right] \mathrm{d}A. \quad \text{(S9)}$$

This Hamiltonian is dependent on the membrane shape, phase, and phase-curvature coupling integrated across the membrane area (A). The first three terms incorporate the local bending modulus (κ), Gaussian modulus (κ_G), mean curvature (c), spontaneous curvature (c_0), and surface tension (λ) of the membrane to consider the energy stored in the membrane shape. Because this work focuses on changes to the phase distribution across the membrane of a static membrane shape (Fig. S5), these first three terms were excluded from the simulations. The next three terms consider the local phase of the membrane (ϕ) with energetic contributions determined by the Landau phase constants (A_L, B_L, and C_L). The final term is an explicit incorporation of the first-order phase-curvature coupling, represented by the modulus (γ). The phase-dependent bending rigidity is incorporated within γ as one of the possible physical explanations of a phase-curvature coupling and a non-zero value for γ. The Landau phase constants A_L, B_L, and C_L enable modeling the phase separation away from the critical point where first-order phase transitions are expected. We set A_L = -1, B_L = 0.7, and C_L = 4; a minimum H was observed on flat membranes (*i.e.*, c = 0) at ϕ= $\pm 8^{-1/2}$ when the phases were well separated with minimal contact length (*i.e.*, small $(\Delta\phi)^2$). Positive values of γ sorted positive values of ϕ to the curvature, which we labeled as L_d. A time step of our simulation included minimizing H by small changes to ϕ equal to -0.05 x ∂H/∂ϕ on location of the membrane. The membrane was divided into a continuum of 1 nm^2 cells. Thermal fluctuations were modeled as the addition of a normal distribution of random perturbations to ϕ. The standard deviation of this noise distribution (σ) corresponds to temperature (T), which was calibrated by qualitative matching of the experimental observations; flat bilayers displayed no stable phase separation at σ = 0.08, but large phase domains were present at σ = 0.07; we observed a qualitative similarity between these two σ values and mixed lipid experiments conducted at T = 15 °C and 35 °C, respectively. Additionally, the perimeter of each simulation ($r \geq 150$ nm) was rescaled each time step to have a $\langle\phi\rangle$ = 0 to prevent the simulation from becoming a single large domain of one phase at low temperatures. Movies of the phase dynamics and a static image of the average phase separation on flat and curved membranes are provided in the Supporting Information with varying T and γ (Movie S1 and Fig. S6)

S.14 Coarse-grained molecular dynamics simulations

Coarse-grained (CG) Martini (43) simulations were performed with the GROMACS 2020 package (65) with full hydration, and 10% of the solvent was modeled as the antifreeze particles to prevent the well-known crystallization of the solvent in the Martini force field (43). The curved membranes were generated by the BUMPy script (42) and maintained by dummy particles that repelled the acyl chains. The dummy participles maintained a hemispherical bud of 5 nm radius connected to a planar bilayer *via* a neck of minimum 5 nm radius of curvature. The dummy particles apply a force on the membrane to maintain its shape mostly by pressing down on the top leaflet of the planar perimeter and pressing up on the bottom leaflet under the membrane bud. The dummy particles were necessary to maintain the

rotationally symmetric membrane bud with a planar perimeter; this shape could not be made through compressing the bilayer as has been employed to create membrane ripples (66). The dummy particles reduce the membrane shape fluctuations, but seemingly allow for free diffusion of individual lipids and the collective diffusion of the lipid phases relative to the membrane curvature, which is the focus of this study.

The two compositions simulated were (1) pure POPC (4497 lipids and 148605 water beads) and (2) a phase separated mixture of 2175 disorder-preferring 1,2-dilinoleoyl-sn-glycero-3-phosphocholine (DLiPC), 2216 order-preferring DPPC, and 1524 cholesterol molecules with 158227 water beads. The systems were simulated at 37 °C for 20 μs, of which the final 10 μs were included in the analyses. Five replicates were performed for the ternary lipid mixture. The molecular trajectories are freely available for download (67, 68). Analysis of the CG results included tracking each lipid type while mimicking the analysis procedure performed on the experimental data, including adding a radial localization imprecision (σ_r) designed to mimic the experimental localization uncertainty. Because the bud radius in experimental systems is 10x larger than that in CG simulations, the most interesting comparisons are that with a Δt that was 1000x longer (*i.e.*, 2 ms vs. 20 μs) and σ_r that was 10x larger (*i.e.*, 20 nm vs. 2 nm) in experiments than simulations. The analysis was also repeated using a novel, geodesic distance-based algorithm to compute Mean Square Displacements instead of the 3D or projected 2D displacements. In this method, the lipids were separated into leaflets. Due to its high rate of flip-flops, cholesterol molecules were excluded from the analysis. Triangular mesh surfaces were created based on the individual leaflets with triangle sizes smaller than 0.8 nm, and the last 10 μs of lipid displacements were mapped onto the surface. Finally, the corresponding geodesic distances were computed. For further details of the method, see reference (50).

Supplemental Figures

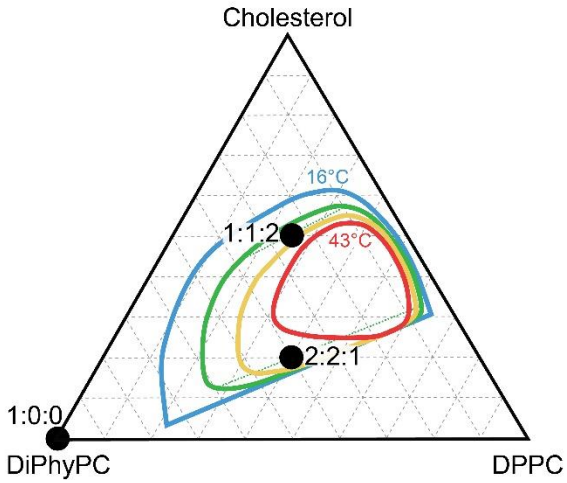

Figure S1:
Lipid bilayers composed of mixtures of DiPhyPC, DPPC, and cholesterol displayed two coexisting liquid phases at select compositions. The mixtures of DiPhyPC:DPPC:cholesterol used in this study are shown (*black dots*). The 16 °C (*blue*) and 43 °C (*red*) phase boundaries were measured previously via fluorescence microscopy of GUVs (69). The boundary of liquid phase coexistence at 25 °C (*green*) and 34 °C (*yellow*) were approximated. At 25 °C, the tie-line (*green dotted*) is longer for the composition of 2:2:1 than 1:1:2, indicating a greater difference between the coexisting liquid phases for 2:2:1 vs. 1:1:2. This figure is adapted from our prior publication, Ref. (34).

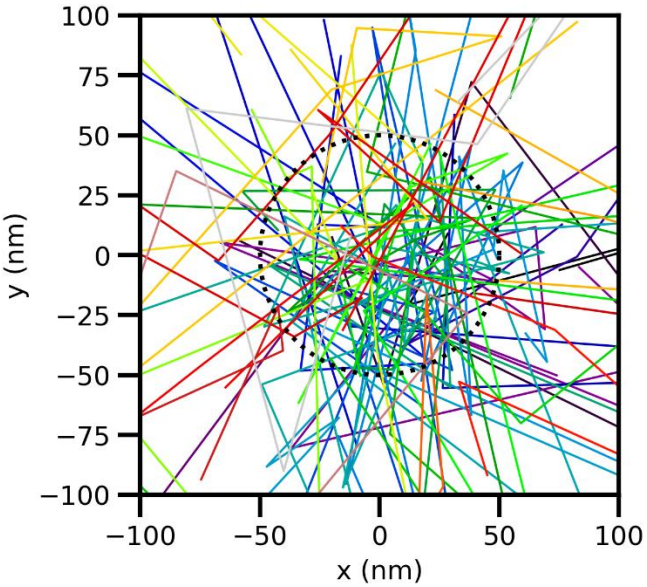

Figure S2:
The membrane draped over the nanoparticles upon the coverslip yields membrane buds connected to the planar SLB. This is demonstrated by fluorescence recovery after photobleaching (26, 55) and single-lipid trajectories. Single-lipid trajectories, such as those shown here, traverse between the planar SLB and the membrane over the nanoparticle.

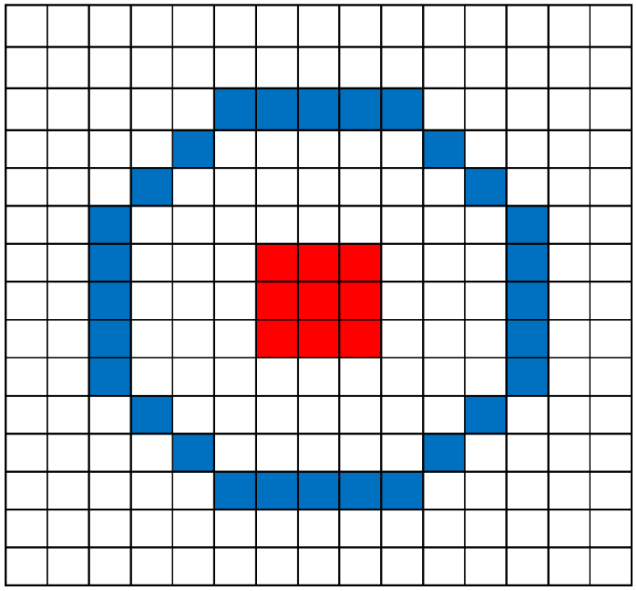

Figure S3:
Diffraction-limited images were used to assess the sorting of disorder-preferring fluorescent lipids to the curved membranes. The curvature center was identified by the colocalization of the fluorescent nanoparticle and the increase in fluorescent lipids in the XY-projected image. Grid shown here was overlaid with the projected image of fluorescent lipids to measure the brightness of the curvature and the brightness of the surrounding, flat membrane. The center 9 pixels (*red*) were deemed to be equal to the curved membrane and the pixels that were closest to 400 nm from the nanoparticle center were deemed equal to the surrounding flat membrane (*blue*). Each pixel maps to 80 nm x 80 nm of the sample.

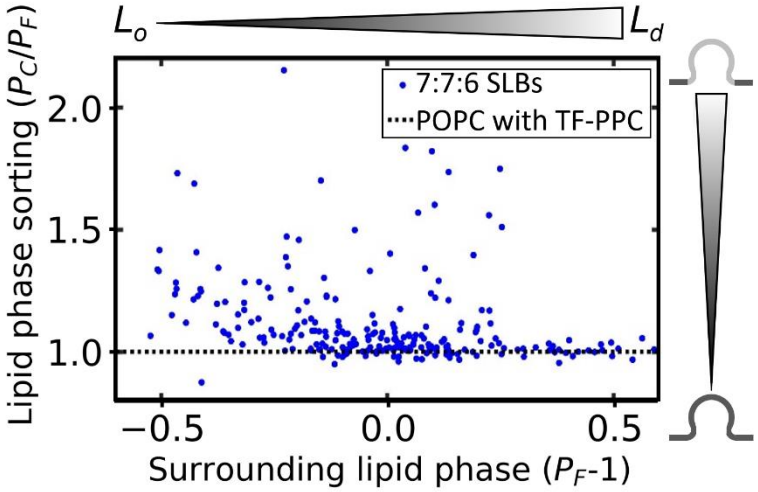

Figure S4:
Curvature-induced lipid phase sorting was confirmed in SLBs made with a 7:7:6 molar ratio of DOPC:DPPC:cholesterol and labeled with the fluorescent lipid TopFluor-PPC, which concentrates in disordered lipid phases. P_C/P_F was greater than 1, indicating that disorder-preferring lipids sorted to the curved membranes. Similar to Fig. 3C in the main text, the curvature-induced sorting was most significant for curvature regions that were immediately surrounded by order-preferring lipids; P_C/P_F decreased with increasing P_F.

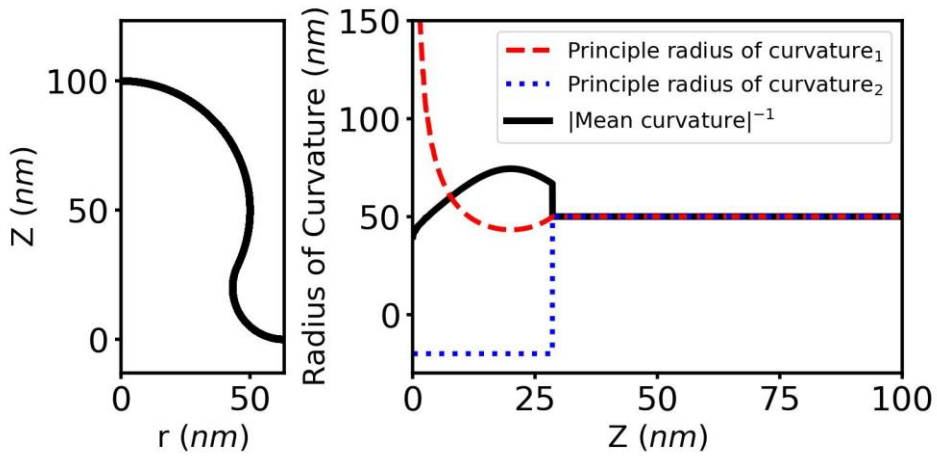

Figure S5:
Continuum simulations of membrane phase and Monte Carlo simulations of lipid diffusion occurred on the azimuthally symmetric membrane shape shown here. The spherical bud top includes a 50-nm radius of curvature. The bud neck smoothly connects the spherical top to the planar surroundings with a minimum 20-nm radius of curvature. This shape is also the best estimate of the experimental membrane shape over the 50-nm radius nanoparticles.

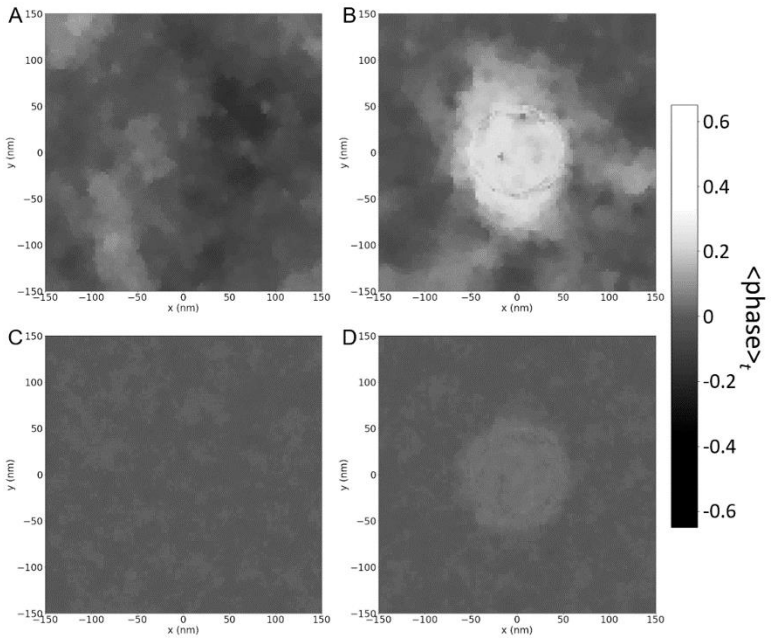

Figure S6:
The continuum simulations include phase fluctuations and sorting of the disordered phase to the center, curved membrane with a balance of the Landau phase constants, phase-curvature coupling, and thermal fluctuations. Shown here is top-view of the time-averaged membrane phase (ϕ), as indicated by the gray-scale. These simulations included (A, B) cold (σ = 0.07) and (C, D) hot (σ = 0.08) membranes that are (A, C) flat or (B, D) with a 50-nm radius membrane bud with a phase-curvature coupling (γ) of 0.1. The time-averaged images shown here are time-averaged; single time points are shown in Fig. 4 and Movie S1.

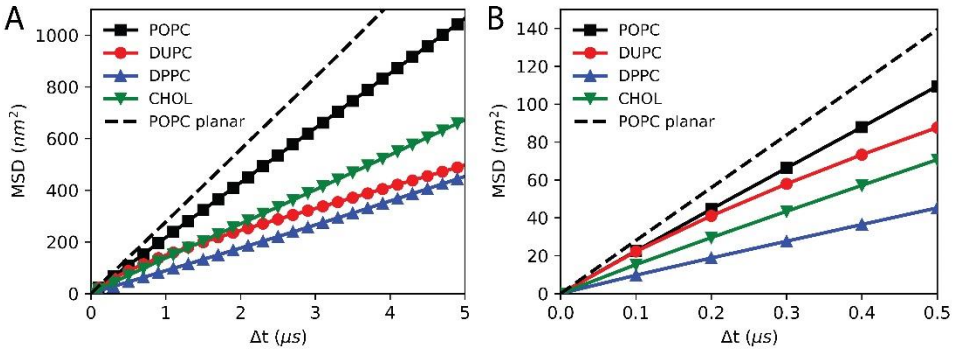

Figure S7:
A conventional mean squared displacement (MSD) vs. Δt analysis of the CG lipid diffusion on the membrane bud, unless otherwise noted. Simulations with periodic boundary conditions were unwrapped to ensure all lipid trajectories were intact before linking and analysis. The presence of the membrane curvature resulted in a non-Brownian (*i.e.,* non-linear) MSD vs. Δt$. The averaging of many long trajectories into each of these data sets resulted in the curved and planar lipid mobility incorporated into these curves such that extracting the lipid diffusion on the curved vs. flat membrane was impossible. (B) shows the zoom of (A) at short Δt values.

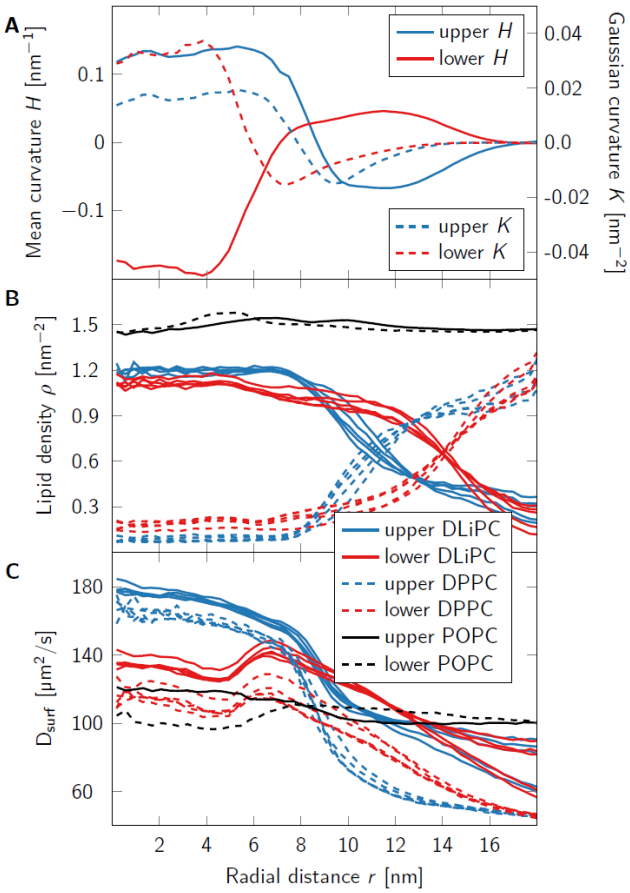

Figure S8:
Geodesic distance-based analysis of lipid displacements in the CG simulations of DLiPC, DPPC, and cholesterol. (A) Leaflet-wise mean (*H*) and Gaussian (*K*) curvatures of the simulated membrane bud. (B) The on-surface densities of POPC, DPPC, and DLiPC lipids, as observed in the individual leaflets, allow the determination of membrane composition in regions of various curvature (*C*) The diffusion coefficient

through the modeled membrane surface (D_{surf}) was computed from displacements at t = 1 ns highlights the differences between lipid diffusivity in the upper and lower membrane leaflets. Budding membranes also possess mean curvature whose sign is conventionally taken as positive if the membrane bends locally away from the outer leaflet. Because this definition is ill-defined for non-closed surfaces, here, a leaflet-wise approach was adopted: the mean curvature of a leaflet was positive when the membrane curved away from the lipid head groups. Using this definition, the mean curvature correlated with the Gaussian curvature in absolute value, but it had different signs for the upper and lower leaflets.

Supplemental Movies

Movie S1:

The phase dynamics at (A, B) cold (σ= 0.07) and (C, D) hot (σ = 0.08) on (A, C) flat and (B, D) curved membranes as governed by Eq. S9. Snapshots of (B, D) are shown in Fig. 4. The static curved membrane shape in (B, D) is shown in Fig. S5.

Movie S2:

Trajectories of a mixed DLiPC, DPPC, and cholesterol within a fixed membrane topography subjected to the Martini force field. The colors of each lipid and bead type are shown in Fig. 5. Each frame here corresponds to 100 ns of simulation time.

Supplemental Tables

Table S1:

Diffusion results for varying membrane compositions, temperatures, and phases. The D_F uncertainties are from the standard deviation D_{xy} values for r between 400 and 600 nm. The D_C/D_F and uncertainties are from the propagated error of D_C and D_F fitting. The listed membrane compositions are the molar ratios of DiPhyPC:DPPC:Cholesterol, unless otherwise stated.

Composition	T (°C)	Phase	Num. of samples	D_F (μm²/s)	D_C/D_F
POPC	25	L_α	12	2.6 ± 0.03	0.4 ± 0.1
DiPhyPC (1:0:0)	17	L_α	19	1.03 ± 0.03	1.2 ± 0.4
DiPhyPC (1:0:0)	36	L_α	18	1.75 ± 0.03	0.7 ± 0.4
1:1:2	19	L_o	8	0.78 ± 0.04	2.3 ± 1.7
1:1:2	19	L_d	8	0.74 ± 0.13	2.1 ± 1.4
1:1:2	27	L_o	14	1.27 ± 0.09	1.5 ± 0.5
1:1:2	27	L_d	8	1.28 ± 0.07	1.3 ± 0.4
1:1:2	37	L_o	11	1.44 ± 0.09	1.4 ± 0.5
2:2:1	17	L_o	11	0.67 ± 0.04	1.7 ± 0.7
2:2:1	17	L_d	14	0.57 ± 0.06	2.3 ± 1.0
2:2:1	27	L_o	10	1.19 ± 0.06	1.1 ± 0.7
2:2:1	27	L_d	16	1.37 ± 0.03	1.5 ± 0.6